Microtubules coordinate protrusion-retraction dynamics in migrating dendritic cells

Aglaja Kopf[1], Jörg Renkawitz[1,2], Robert Hauschild[1], Irute Girkontaite[3], Kerry Tedford[4], Jack Merrin[1], Oliver Thorn-Seshold[5], Dirk Trauner[6], Hans Häcker[7], Klaus-Dieter Fischer[4], Eva Kiermaier[1,8,*] and Michael Sixt[1,*]

[1]Institute of Science and Technology (IST) Austria, 3400 Klosterneuburg, Austria.

[2]Biomedical Center (BMC), Institute of Cardiovascular Physiology and Pathophysiology, Ludwig Maximilian University (LMU) Munich, 81377 Munich, Germany.

[3]Department of Immunology, State Research Institute Centre for Innovative Medicine, LT-08409 Vilnius, Lithuania.

[4]Institute of Biochemistry and Cell Biology, Otto von Guericke University, 39120 Magdeburg, Germany.

[5]Department of Pharmacy, Ludwig Maximilian University (LMU) Munich, 81377 Munich, Germany.

[6]Department of Chemistry, New York University, New York, NY 10003, USA.

[7]Department of Infectious Diseases, St. Jude Children's Research Hospital, Memphis, TN 38105, USA.

[8]Life and Medical Science (LIMES) Institute, University of Bonn, 53113 Bonn, Germany.

*Correspondence to Michael Sixt; Sixt@ist.ac.at, phone +43 2243 90003801 or Eva Kiermaier ekiermai@uni-bonn.de, phone +49 228-73-62819

Abstract

When traversing complex microenvironments, migrating cells extend multiple exploratory protrusions into the interstitial space. In order to preserve cell integrity and maintain polarity as the cell advances, supernumerary protrusions and tethered trailing edges need to be retracted in a coordinated fashion. Here, we demonstrate that spatially distinct microtubule dynamics regulate cell migration by locally specifying the retraction of explorative protrusions. We found that in migrating dendritic cells, local microtubule depolymerization triggers myosin II dependent contractility via the RhoA GEF Lfc. Depletion of Lfc leads to aberrant myosin localization, thereby causing two effects that rate-limit locomotion: i) defective adhesion-resolution and ii) impaired cell edge coordination during path-finding. Such compromised cell shape coordination is particularly hindering when cells navigate through geometrically complex microenvironments, where it leads to entanglement and ultimately fragmentation of the cell body. Our data demonstrate that microtubules regulate dendritic cell shape and coherence by local control of protrusion-retraction dynamics.

Introduction

Cellular trafficking is fundamental for diverse physiological processes such as morphogenesis and immune surveillance (Friedl and Wolf, 2010; Haston et al., 1982; Weijer, 2009). The active locomotion of single cells relies on the dynamic integration of cytoskeletal polymers, including actin, microtubules, and intermediate filaments. Hence their regulators have to be orchestrated in a spatiotemporally coordinated manner (Abercrombie et al., 1970; Horwitz and Parsons, 1999; Petrie and Yamada, 2012; Waterman-Storer and Salmon, 1997). During directed migration, cells adopt a polarized conformation with actin-rich lamellipodia at the leading edge and a contractile trailing edge. The actin cytoskeleton acts as the major force generator: polymerization pushes out the leading edge and actomyosin complexes provide contractility to propel the cell body and retract the trailing edge (Krause and Gautreau, 2014; Mitchison and Cramer, 1996). By contrast, the contribution of the microtubule (MT) cytoskeleton to force-generation is limited and most effects are exerted indirectly via regulation of the actomyosin system (Etienne-Manneville, 2013; Mogilner and Oster, 2003). Typically, MTs nucleate radially from microtubule organizing centers (MTOCs), with slow-growing minus ends anchored at the centrosome. Fast-growing plus ends project to the cell periphery where they undergo stochastic transitions of growth (polymerization) and shrinkage (catastrophe), referred to as dynamic instability (Brouhard, 2015; Desai and Mitchison, 1997; Mitchison and Kirschner, 1984). The MT and actin networks crosstalk at many levels, and in fibroblasts, it was shown that polymerizing MTs impede contractility but promote leading edge extension via activation of Rac (Waterman-Storer et al., 1999). Conversely, MT depolymerization triggers activation of the contractile module by regulating activators of Rho family GTPases, such as RhoA-specific guanine nucleotide exchange factors (RhoGEFs) (Ridley, 2003; Wittmann and Waterman-Storer, 2001). RhoA activates Rho-associated kinase (ROCK), leading to phosphorylation of myosin light chain (MLC), which mediates the formation of contractile actin stress fibers (Amano et al., 1996).

Leukocytes, including dendritic cells (DCs), rely on dynamic cytoskeletal rearrangements to allow for high migration velocities and rapid responses to changes in environmental cues (Sanchez-Madrid and Del Pozo, 1999; Vargas et al., 2017; Vicente-Manzanares and Sánchez-Madrid, 2004). DCs reside in peripheral tissues throughout the mammalian organism and upon pathogen encounter mature from an antigen-capturing to an antigen-presenting state. These cells become highly motile during activation, migrate along chemokine gradients towards afferent lymphatic vessels and finally reach the draining lymph node where priming of naïve T cells is initiated (Banchereau and Steinman, 1998). DCs are one of the best-developed paradigms to study amoeboid polarization, since locomotion and

51 the basic patterns of actomyosin and adhesion dynamics are beginning to be understood *in*
52 *vitro* and *in vivo* (Heuzé et al., 2013; Vargas et al., 2017). However, in comparison to what is
53 known about actin dynamics during leukocyte migration, the role of MT reorganization is
54 poorly understood (Eddy et al., 2002; Niggli, 2003; Yoo et al., 2012).
55 Here, we investigate MT-mediated processes that govern DC shape and motility. We
56 describe a mechanism by which local modulation of MT dynamics controls both, de-
57 adhesion of cell attachment sites and retraction of entangled protrusions, thereby ensuring
58 that the advancing cell body maintains its morphological coherence.

Results

Microtubules control dendritic cell polarity

To evaluate whether MTs are required for DC migration in physiological environments, we employed mouse ear explants (Supplementary figure 1A). In this system, endogenous DCs undergo maturation, up-regulate the chemokine-receptor 7 (CCR7) and subsequently migrate along an interstitial gradient of the CCR7 ligand CCL21 towards afferent lymphatic vessels (Ohl et al., 2004; Weber et al., 2013). We treated split ears with the MT-destabilizing drug Nocodazole and determined the distance between MHCII expressing mature DCs and lymphatic vessels (Figure 1A). Compared to control conditions (DMSO), mean distances were significantly increased by Nocodazole, and the same was true when *in vitro* generated mature DCs were allowed to migrate into ear explants (Supplementary figure 1B), suggesting a critical role for MTs during DC migration. To isolate specific effects of MT depolymerization, we *in vitro* reconstituted DC locomotion along chemotactic gradients in a succession of reductionist environments (Supplementary figure 1A). In three dimensional (3D) collagen matrices (Sixt and Lämmermann, 2011), which largely mimic the geometrically complex dermal interstitium, both migration speed and directionality were significantly reduced upon Nocodazole treatment (Figure 1B, C, and supplementary figure 1C). Under a pad of agarose where cells are physically confined between top and bottom surfaces ("2,5D") but have free directional choice in the plane of migration (Supplementary figure 1A) (Heit and Kubes, 2003; Lämmermann et al., 2009; Renkawitz et al., 2009), Nocodazole-treatment caused a substantial drop in directional persistence (Figure 1D, E) and cells displayed a rounded morphology and oscillatory protrusion dynamics (Figure 1F). However, velocities were largely unperturbed (Figure 1G) in the absence of filamentous tubulin (Supplementary figure 1D, E). These data suggest that MT depolymerization causes a defect in polar organization rather than actual locomotion, a phenomenon previously observed upon genetic disruption of the GTPase Cdc42, which causes DCs to "entangle" in complex 3D environments but still allows them to migrate in open spaces (Harada et al., 2012; Lämmermann et al., 2009). To challenge this presumption we placed DCs in linear channels, where a polarized shape is enforced by the 1D geometry of the environment, allowing the cells to make binary directional choices only. Here, Nocodazole treatment mildly reduced instantaneous migration velocities but caused a major defect in persistence as cells frequently switched direction (Figure 1H-J and supplementary figure 1F). Together, these data indicate that elimination of MTs preserves the locomotive ability of DCs driven by actomyosin, but causes profound changes in the polar organization that prevent efficient navigation through complex 3D environments.

94

95 **Microtubules control polar cellular organization via the contractile module**

96 The rounded cell morphologies and directional oscillations of Nocodazole-treated cells
97 prompted us to measure parameters of cellular contractility. We found that Nocodazole
98 treatment led to increased activation of RhoA (Figure 2A) and phosphorylation of MLC
99 (Figure 2B). This effect was reversed when Rho-associated protein kinase (ROCK) activity
100 was pharmacologically blocked using Y27632, suggesting that MTs control cell polarity by
101 regulating contractility.

102 Therefore, we tested whether ROCK inhibition on Nocodazole-treated cells would rescue
103 Nocodazole-induced migratory defects. We again employed the previously used succession
104 of reductionist experimental setups, which allowed us to separate the impact on locomotion
105 versus polarity. In 3D collagen gels, double-treatment with Nocodazole and Y27632 did not
106 rescue the migratory defect and cells slowed down even more than upon Nocodazole-only
107 treatment and often fragmented at their peripheral protrusions (Figure 2C, D and
108 supplementary movie 1). Under agarose, the detrimental effect of Nocodazole on polarized
109 (eccentric) cell shape was rescued, while migration velocities were still reduced (Figure 2E-
110 G, supplementary figure 1G). Interestingly though, in 1D channels inhibition of ROCK largely
111 rescued the oscillatory behavior and also improved locomotion speed of Nocodazole-treated
112 cells (Figure 2H-J and supplementary movie 2). These data suggest that in DCs, global MT
113 depolymerization causes hyperactivity of the contractile module via spatially uncontrolled
114 activation of RhoA and ROCK, leading to oscillations of the contractile trailing edge. Blocking
115 ROCK restores persistent locomotion in 1D channels, in which protrusion coordination is not
116 rate-limiting for migration as the configuration of the environment extrinsically dictates cell
117 shape. By contrast, in complex geometries, where cells need to coordinate cell edge
118 dynamics in order to translocate efficiently (Lämmermann et al., 2009), ROCK inhibition did
119 not rescue locomotion. These findings indicate that global MT depolymerization induces
120 spatially uncontrolled hypercontractility and locally coordinated contractility becomes more
121 rate-limiting for locomotion within increasing geometrical complexity of the environment.

122

123 **Polarized microtubule dynamics locally activate the contractile module**

124 The nocodazole-induced contraction around the entire cell perimeter led us to investigate if
125 local MT depolymerization serves to spatially instruct contractile-events. In order to evaluate
126 if MT dynamics are compatible with the concept of local MT depolymerization causing local
127 retraction, we first mapped MT filaments in migrating DCs. When cells were fixed upon
128 migration under agarose (Supplementary figure 2A, lower panel), MTs polarized along the

129 axis of migration with highest signal intensities in trailing edge regions (Figure 3A) and a
130 lower density of MTs protruding towards the leading edge (Figure 3A grey inset). Testing co-
131 localization between peak intensities of alpha- and gamma-tubulin revealed that the
132 centrosome acts as the primary MTOC (Supplementary figure 2B) and that the MTOC was
133 preferentially located behind the nucleus (Figure 3B). To analyze MT dynamics, we co-
134 transfected DCs with tubulin-GFP and end-binding protein 3 (EB3)-mCherry (Supplementary
135 movie 3 and supplementary figure 2C). Automated analysis of signal trajectories (Matov et
136 al., 2010) showed that MT growth occurs across the entire cell area (Supplementary figure
137 2D) and angular distribution revealed highly polarized growth along the anterior-posterior
138 axis (Figure 3C and supplementary figure 2E-G). Notably, back-directed MTs frequently
139 underwent catastrophic events (switch from growth to shrinkage) and rapidly disassembled
140 towards the MTOC (Figure 3D, supplementary figure 2H and supplementary movie 4). By
141 contrast, front-directed MTs hardly ever underwent shrinkage but instead continuously grew
142 into protruding areas (Figure 3D). To substantiate these findings, we stained fixed migratory
143 DCs for the stabilizing acetylation modification and found that front-oriented were acetylated,
144 but back oriented MTs had substantially lower levels of acetylation (Figure 3E), irrespective
145 of MTOC positioning (Supplementary Figure 2I). Together, we find increased dynamism and
146 high catastrophe-frequency of trailing edge directed MTs.
147 To directly test for a potential causal link between MT depolymerization and local activation
148 of the contractile module, we devised a photo-pharmacological approach to depolymerize
149 MTs in migratory cells with spatiotemporal control. We used Photostatin-1 (PST-1), a
150 reversibly photo-switchable analog of combretastatin A-4, one of the most prominent MT
151 inhibitors. This compound can be functionally toggled between the active and inactive state
152 by blue and red light, respectively (Borowiak et al., 2015). To validate the approach, we
153 locally activated the drug and simultaneously visualized MT dynamics using EB3-mCherry.
154 We found that local photo-activation triggered an almost instantaneous disappearance of the
155 EB3 signal in the presence but not in the absence of Photostatin (Figure 3F), indicating
156 immediate stalling of MT polymerization. Local photoactivation in protruding areas of the cell
157 consistently led to the collapse of the respective protrusion and subsequent re-polarization
158 (Figure 3G, H and supplementary movie 5). This response was only observed in the
159 presence of Photostatin, while cells were refractory to illumination in the absence of the
160 drug. These data demonstrate a causal relationship between MT depolymerization and
161 protrusion-retraction cycles. This effect can act locally within a cell, raising the possibility that
162 MTs coordinate subcellular retractions when cells navigate through complex environments
163 such as collagen gels or a physiological interstitium.

164 **Accumulation of Lfc precedes cellular retraction**

165 One potential link between MT depolymerization and cell contractility is the RhoA specific
166 GEF Lfc (the murine homolog of GEF-H1). Lfc is inactive when bound to MTs, whereas MT
167 depolymerization triggers its release and subsequent activation of the contractile module via
168 RhoA and its effectors ROCK and MLC kinase in other cell types (Chang et al., 2008;
169 Graessl et al., 2017; Krendel et al., 2002; Ren, 1998).

170 We first mapped Lfc distribution by visualizing a Lfc-GFP fusion protein (Supplementary
171 movie 6). Immunofluorescence of alpha-tubulin in Lfc-GFP-expressing cells confirmed
172 localization of Lfc to MTs (Krendel et al., 2002) (Supplementary figure 3A), with the highest
173 signal in trailing edge areas (Figure 4A, purple arrowhead and B). Besides its clear
174 filamentous appearance across the cell, Lfc-GFP accumulated as a diffuse patch in trailing
175 edges and in retracting protrusions (Figure 4B, supplementary figure 3B and supplementary
176 movie 6). Treatment with Nocodazole globally changed Lfc distribution from filamentous to
177 diffuse (Supplementary figure 3C). To test whether Lfc accumulates in actively retracting
178 areas, we determined the spatiotemporal co-localization of Lfc and MLC by imaging double-
179 transfected cells migrating under agarose. Time course analysis revealed that both proteins
180 are strongly polarized in trailing edge regions and at the cell center in close proximity to the
181 nucleus during phases of cell body translocation. Correlation coefficients of Lfc and MLC in
182 retracting areas were positive over time, indicating that locally increased Lfc levels are
183 paralleled by increased MLC signal intensities in these regions (Figure 4C). Accordingly,
184 quantitative analysis of signal distribution dynamics within sub-cellular compartments
185 revealed a strong increase in Lfc signal before the onset of membrane retraction (Figure
186 4D). This pattern was particularly prominent when we placed DCs in “pillar forests”, in which
187 cells - confined between two surfaces - navigate through an obstacle course of pillars along
188 a chemokine gradient (Renkawitz et al., 2018) (Supplementary figure 1A). Here, the MTOC
189 moved in a remarkably straight path towards the gradient, while Lfc-GFP transiently
190 accumulated in peripheral explorative protrusions and at the trailing edge (Figure 4E and
191 supplementary movie 7). Together, these data show that Lfc associates with MTs and locally
192 accumulates, together with MLC, at sites of retraction.

193

194 **Lfc specifies myosin localization at the trailing edge**

195 To gain insight into the localized impact of Lfc on contractile activity, we mapped subcellular
196 MLC dynamics over time. While MLC was largely excluded from the leading lamellipodium,
197 two distinct pools were detectable in the cell body of wild-type cells: one at the trailing edge
198 and one in the cell center, at the base of the lamellipodium and around the nucleus (Figure

199 5A). Intensities of trailing edge MLC strongly increased during fast directional migration,
200 whereas the central pool was maintained independently of migratory speed (Figure 5B, C,
201 supplementary figure 3D-F, and supplementary movie 8). Upon Nocodazole treatment the
202 trailing edge MLC signal was weakened relative to the perinuclear pool, which displayed
203 dynamic back-to-front oscillations (Figure 5D and supplementary figure 3G and
204 supplementary movie 8).
205 To test for the contribution of Lfc on MLC positioning in DCs, we generated *lfc*-deficient mice
206 (Supplementary figure 4A-D) and found that DCs derived from *lfc*$^{-/-}$ bone marrow precursor
207 cells differentiated and matured normally as revealed by flow cytometry of surface markers
208 (Kamon et al., 2006) (Supplementary figure 4E, F). *Lfc*-deficient cells displayed a stable
209 lamellipodium. The MTOC localization and MT distribution were indistinguishable from wild-
210 type cells (Supplementary figure 4G-I). Strikingly, *lfc*$^{-/-}$ DCs completely lacked MLC
211 accumulation at the trailing edge but maintained the pool in the cell center (Figure 5E, F,
212 supplementary figure 3H, I and supplementary movie 8). We measured the same
213 localization pattern of the active form of endogenous MLC (phospho-MLC) in fixed samples
214 (Figure 5G and supplementary figure 3J, K). Biochemical analysis revealed reduced but not
215 eliminated RhoA and pMLC levels in *lfc*$^{-/-}$ DCs (supplementary figure 4J, K). We next
216 performed quantitative morphometry of immunostainings for moesin, the major ERM (ezrin-
217 radixin-moesin) protein expressed in DCs and a typical component of the leukocyte trailing
218 edge (often termed uropod). Moesin was partially lost from the trailing edge of *lfc*-deficient
219 DCs (Figure 5H) and biochemical analysis confirmed reduced phospho-ERM levels (Figure
220 5I). Together, these data indicate that MTs control the positioning of the contractile module
221 via Lfc and that the functional organization of the trailing edge is selectively perturbed in the
222 absence of *lfc*.
223
224 **Lfc controls DC migration by regulating MT-mediated adhesion resolution**
225 We next measured the migratory capacity of *lfc*$^{-/-}$ DCs. *In situ* migration in explanted ear
226 sheets showed that *lfc*$^{-/-}$ cells reached the lymphatic vessels later than control cells (Figure
227 6A) and chemotaxis of *lfc*$^{-/-}$ DCs in collagen gels was substantially impaired (Figure 6B).
228 Inhibition of ROCK led to a further drop in migratory speed in both control and *lfc*$^{-/-}$ cells,
229 arguing for additional - Lfc-independent - modes of ROCK activation. When we measured
230 cell length in 3D collagen gels (Figure 6C, D) and under agarose (Figure 6E), migrating *lfc*$^{-/-}$
231 DCs were significantly elongated compared to control cells, indicating retraction defects.
232 In cells that employ an amoeboid mode of migration, trailing edge retraction is essential in
233 two non-exclusive ways: i) under conditions where cells adhere to surfaces, retraction forces

234 are required to disassemble integrin adhesion sites and ii) in complex 3D environments the
235 cell has to eventually retract all but one of its exploratory protrusions in order to not get
236 stalled by entanglement ((Lämmermann et al., 2009), Renkawitz et al., under revision).
237 We first tested the role of adhesion-resolution in under agarose assays, where, depending
238 on the surface conditions, DCs can flexibly shift between adhesion-dependent and
239 adhesion-independent locomotion (Renkawitz et al., 2009). Under adhesive conditions *lfc*$^{-/-}$
240 DCs were elongated compared to wild-type cells (Figure 6E) and this elongation was lost
241 when the migratory substrate at the bottom was passivated with polyethylene glycol (PEG)
242 (Figure 6F). When cells on adhesive surfaces were treated with Nocodazole, wild-type cells
243 shortened, as expected due to hypercontractility. Notably, *lfc*$^{-/-}$ DCs elongated even more
244 upon treatment with Nocodazole (Supplementary movie 9), indicating that elimination of Lfc-
245 mediated hypercontractility unmasked additional modes of MT-mediated length control.
246 Elongation of *lfc*$^{-/-}$ cells by Nocodazole was also largely absent on PEG-coated surfaces.
247 Importantly, not only morphological, but also migratory parameters were restored on
248 passivated surfaces (Figure 6 G, H). Together, these data demonstrate that whenever DCs
249 migrate in an adhesion-mediated manner, MTs control de-adhesion and this is partially
250 mediated via Lfc and myosin.
251
252 **Microtubules mediate retraction of supernumerary protrusions via Lfc**
253 In 3D collagen gels adhesion plays a minor role (Friedl et al., 2012; Lämmermann et al.,
254 2008; van Helvert et al., 2018). Therefore, elongation of *lfc*$^{-/-}$ DCs suggested that cells might
255 entangle rather than fail to de-adhere. To directly address this option, we used a microfluidic
256 setup, in which DCs migrate in a straight channel towards a junction where the channel
257 splits into four paths. In this setup DCs initially insert protrusions into all four channels before
258 they retract all but one protrusion and thereby choose one path (Supplementary figure 4L,
259 M). We could show previously that passage of the MTOC through the junction marks the
260 time-point of retraction and that both MT depolymerization and myosin II inhibition
261 substantially increase passage times due to retraction failure (Renkawitz et al., under
262 revision). In line with the finding that Lfc mediates between MTs and myosin II, *lfc*$^{-/-}$ DCs
263 also showed increased passage times and defective retraction of supernumerary protrusions
264 (Figure 7A, B). Notably, *lfc*$^{-/-}$ DCs often advanced through more than one channel, ultimately
265 resulting in auto-fragmentation into migratory cytoplasts (Figure 7C, D and supplementary
266 movie 10). When DCs migrated through channels with single constrictions, *lfc*$^{-/-}$ cells passed
267 with the same speed and efficiency as wild-type cells (Figure 7E and supplementary figure
268 4N), demonstrating that not the actual passage through one constriction was perturbed but

269 rather the coordination of competing protrusions. These data indicate that in complex 3D
270 geometries, where the cell has to choose between different paths, MTs - via Lfc and myosin
271 II - specify entangled protrusions for retraction.
272 To test for possible effects of Lfc beyond adhesion resolution and protrusion coordination,
273 we placed DCs in straight 1D channels, where neither trailing edge adhesion nor
274 entanglement are rate-limiting. Here, the hypercontractility-caused oscillations triggered by
275 Nocodazole (Figure 1H and 7F) were substantially rescued by knockout of *lfc* (Figure 7F-H).
276 Together, our data indicate that the major role of MT dynamics in migrating DCs is to specify
277 sites of protrusion-retraction and that this is partially regulated by the RhoA GEF Lfc and
278 actomyosin contraction.
279

Discussion

Here we report that MT depolymerization in peripheral regions of migrating DCs locally triggers actomyosin-mediated retraction via the RhoA GEF Lfc. Thereby MTs coordinate protrusion-retraction dynamics and prevent that the cell gets too long or arborized.

How different cell types maintain their typical shape and how cell types with a dynamic shape prevent losing physical coherence is poorly understood. This issue becomes particularly critical in migrating cells, where protrusion of the leading edge has to be balanced by retraction of the tail (Hind et al., 2016) and where multiple protrusions of one cell often compete for dominance, as exemplified in the split pseudopod model of chemotactic migration (Insall, 2010). The two prevalent models of how remote edges of mammalian cells communicate with each other are based on the sensing of endogenous mechanical parameters that in turn control the actomyosin system. In cell types that tightly adhere to substrates via focal adhesion complexes it has been proposed that actomyosin itself is the sensing structure and that adhesion sites communicate mechanically via actin stress fibers: when contractile stress fibers were pharmacologically, physically or genetically perturbed in mesenchymal cells, the cells lost their coherent shape and spread in an uncontrolled manner (Cai et al., 2010; Cai and Sheetz, 2009). A second model suggests that lateral plasma membrane tension, which is thought to rapidly equilibrate across the cell surface, mediates communication between competing protrusions and serves as an input system to control actomyosin dynamics (Diz-Muñoz et al., 2016; Houk et al., 2012; Keren et al., 2008; Murrell et al., 2015).

Based on our findings we propose a third model of shape control, in which MTs take the role of the shape-sensor that signals to actin dynamics. This pathway might be particularly relevant for leukocytes, as they do not develop stress fibers due to low adhesive forces and are often too large and ramified (such as DCs in 3D matrices) to allow equilibration of membrane tension across the cell body (Shi et al., 2018).

Despite being therapeutically targeted, the role of MTs in leukocytes is poorly studied. In neutrophil granulocytes and T cells, it was shown that pharmacological MT depolymerization leads to enhanced cellular polarization, owing to a hypercontractility-induced symmetry break that triggers locomotion but at the same time impairs directional persistence and chemotactic prowess (Redd et al., 2006; Takesono et al., 2010; Xu et al., 2005; Yoo et al., 2012). Although this pharmacological effect might explain the efficacy of MT depolymerizing drugs like Colchicine in the treatment of neutrophilic hyperinflammation, excessive hypercontractility overwrites any morphodynamic subtleties and leaves the question of if

315 MTs contribute to leukocyte navigation under physiological conditions. Our findings
316 demonstrate that in DCs this is indeed the case and that the MT-sequestered RhoA GEF Lfc
317 is an important mediator between MT dynamics and actomyosin driven retraction.
318 Importantly, we show that DCs lacking both Lfc and MTs had even more severe cell shape
319 defects than the ones lacking Lfc only. This demonstrates that Lfc and myosin II are not the
320 only pathways and that MT depolymerization induces cell retraction via additional modes
321 that remain to be identified.
322 Although it is likely that multiple feedbacks signal between actin and MTs, we show that
323 there is a strong causal link between local MT catastrophes and cellular retraction, with MTs
324 acting upstream. This raises the key question how MT stability is locally regulated in DCs.
325 Among many possible inputs (adhesion, chemotactic signals etc.) one simple option might
326 be related to the fact that in leukocytes the MTOC is the only site where substantial
327 nucleation of MTs occurs. In complex environments (like the pillar maze we devised) the
328 MTOC of a DC moves a remarkably straight path, while lateral protrusions constantly
329 explore the environment (Figure 4F). In line with this, passage of the MTOC beyond an
330 obstacle is the decisive event determining the further trajectory of the cell (Renkawitz et al,
331 under revision). Upon passage of the MTOC, sheer geometry might dictate that lateral
332 protrusions are cut off MT supply because the filaments are too inflexible to find their way
333 into narrow and ramified spaces. Hence, it is possible that MTs serve as an internal
334 explorative system of the cell that informs actomyosin whenever a peripheral protrusion
335 locates too distant from the centroid and initiates its retraction.

Acknowledgments

The authors thank the Scientific Service Units of IST Austria for their excellent services. This work was supported by the European Research Council (ERC StG 281556 and CoG 724373), a grant from the Austrian Science Foundation (FWF) and the FWF DK “Nanocell” to M.S., the German Research Foundation (DFG) (SFB1032 project B09, Emmy Noether grant) to O.T.-S. J.R was supported by ISTFELLOW funding from the People Programme (Marie Curie Actions) of the European Union's Seventh Framework P (FP7/2007-2013) under REA grant agreement n° [291734] and an EMBO long-term fellowship (ALTF 1396-2014) co-funded by the European Commission (LTFCOFUND2013, GA-2013-609409). H.H. was supported by the American Lebanese Syrian Associated Charities (ALSAC).

Conflict of interest

The authors declare no competing financial interests.

350 **References**

351 Abercrombie, M., Heaysman, J.E., Pegrum, S.M., 1970. The locomotion of fibroblasts in
352 culture. I. Movements of the leading edge. Experimental Cell Research 59, 393–398.
353 Amano, M., Ito, M., Kimura, K., Fukata, Y., Chihara, K., Nakano, T., Matsuura, Y., Kaibuchi,
354 K., 1996. Phosphorylation and activation of myosin by Rho-associated kinase (Rho-
355 kinase). Journal of Biological Chemistry 271, 20246–20249.
356 Banchereau, J., Steinman, R.M., 1998. Dendritic cells and the control of immunity. Nature
357 392, 245–252. doi:10.1038/32588
358 Borowiak, M., Nahaboo, W., Reynders, M., Nekolla, K., Jalinot, P., Hasserodt, J., Rehberg,
359 M., Delattre, M., Zahler, S., Vollmar, A., Trauner, D., Thorn-Seshold, O., 2015.
360 Photoswitchable Inhibitors of Microtubule Dynamics Optically Control Mitosis and Cell
361 Death. Cell 162, 403–411. doi:10.1016/j.cell.2015.06.049
362 Brouhard, G.J., 2015. Dynamic instability 30 years later: complexities in microtubule growth
363 and catastrophe. Mol. Biol. Cell 26, 1207–1210. doi:10.1091/mbc.E13-10-0594
364 Cai, Y., Rossier, O., Gauthier, N.C., Biais, N., Fardin, M.-A., Zhang, X., Miller, L.W., Ladoux,
365 B., Cornish, V.W., Sheetz, M.P., 2010. Cytoskeletal coherence requires myosin-IIA
366 contractility. Journal of Cell Science 123, 413–423. doi:10.1242/jcs.058297
367 Cai, Y., Sheetz, M.P., 2009. Force propagation across cells: mechanical coherence of
368 dynamic cytoskeletons. Current Opinion in Cell Biology 21, 47–50.
369 doi:10.1016/j.ceb.2009.01.020
370 Chang, Y.-C., Nalbant, P., Birkenfeld, J., Chang, Z.-F., Bokoch, G.M., 2008. GEF-H1
371 couples nocodazole-induced microtubule disassembly to cell contractility via RhoA. Mol.
372 Biol. Cell 19, 2147–2153. doi:10.1091/mbc.E07-12-1269
373 Croft, D.R., Coleman, M.L., Li, S.X., Robertson, D., Sullivan, T., Stewart, C.L., Olson, M.F.,
374 2005. Actin-myosin-based contraction is responsible for apoptotic nuclear disintegration.
375 The Journal of Cell Biology 168, 245–255. doi:10.1083/jcb.200409049
376 Desai, A., Mitchison, T.J., 1997. Microtubule polymerization dynamics. Annu. Rev. Cell Dev.
377 Biol. 13, 83–117. doi:10.1146/annurev.cellbio.13.1.83
378 Diz-Muñoz, A., Thurley, K., Chintamen, S., Altschuler, S.J., Wu, L.F., Fletcher, D.A., Weiner,
379 O.D., 2016. Membrane Tension Acts Through PLD2 and mTORC2 to Limit Actin
380 Network Assembly During Neutrophil Migration. PLoS Biol. 14, e1002474.
381 doi:10.1371/journal.pbio.1002474
382 Eddy, R.J., Pierini, L.M., Maxfield, F.R., 2002. Microtubule asymmetry during neutrophil
383 polarization and migration. Mol. Biol. Cell 13, 4470–4483. doi:10.1091/mbc.E02-04-0241
384 Etienne-Manneville, S., 2013. Microtubules in Cell Migration. Annu. Rev. Cell Dev. Biol. 29,

385 471–499. doi:10.1146/annurev-cellbio-101011-155711
386 Friedl, P., Sahai, E., Weiss, S., Yamada, K.M., 2012. New dimensions in cell migration.
387 Nature Publishing Group 13, 743–747. doi:10.1038/nrm3459
388 Friedl, P., Wolf, K., 2010. Plasticity of cell migration: a multiscale tuning model. The Journal
389 of Cell Biology 188, 11–19. doi:10.1083/jcb.200909003
390 Graessl, M., Koch, J., Calderon, A., Kamps, D., Banerjee, S., Mazel, T., Schulze, N.,
391 Jungkurth, J.K., Patwardhan, R., Solouk, D., Hampe, N., Hoffmann, B., Dehmelt, L.,
392 Nalbant, P., 2017. An excitable Rho GTPase signaling network generates dynamic
393 subcellular contraction patterns. The Journal of Cell Biology 216, 4271–4285.
394 doi:10.1083/jcb.201706052
395 Harada, Y., Tanaka, Y., Terasawa, M., Pieczyk, M., Habiro, K., Katakai, T., Hanawa-
396 Suetsugu, K., Kukimoto-Niino, M., Nishizaki, T., Shirouzu, M., Duan, X., Uruno, T.,
397 Nishikimi, A., Sanematsu, F., Yokoyama, S., Stein, J.V., Kinashi, T., Fukui, Y., 2012.
398 DOCK8 is a Cdc42 activator critical for interstitial dendritic cell migration during immune
399 responses. Blood 119, 4451–4461. doi:10.1182/blood-2012-01-407098
400 Haston, W.S., Shields, J.M., Wilkinson, P.C., 1982. Lymphocyte locomotion and attachment
401 on two-dimensional surfaces and in three-dimensional matrices. The Journal of Cell
402 Biology 92, 747–752.
403 Heit, B., Kubes, P., 2003. Measuring chemotaxis and chemokinesis: the under-agarose cell
404 migration assay. Sci. STKE 2003, PL5–pl5. doi:10.1126/stke.2003.170.pl5
405 Heuzé, M.L., Vargas, P., Chabaud, M., Le Berre, M., Liu, Y.-J., Collin, O., Solanes, P.,
406 Voituriez, R., Piel, M., Lennon-Duménil, A.-M., 2013. Migration of dendritic cells:
407 physical principles, molecular mechanisms, and functional implications. Immunol Rev
408 256, 240–254. doi:10.1111/imr.12108
409 Hind, L.E., Vincent, W.J.B., Huttenlocher, A., 2016. Leading from the Back: The Role of the
410 Uropod in Neutrophil Polarization and Migration. Developmental Cell 38, 161–169.
411 doi:10.1016/j.devcel.2016.06.031
412 Horwitz, A.R., Parsons, J.T., 1999. Cell biology - Cell migration - Movin' on. Science 286,
413 1102–1103.
414 Houk, A.R., Jilkine, A., Mejean, C.O., Boltyanskiy, R., Dufresne, E.R., Angenent, S.B.,
415 Altschuler, S.J., Wu, L.F., Weiner, O.D., 2012. Membrane tension maintains cell polarity
416 by confining signals to the leading edge during neutrophil migration. Cell 148, 175–188.
417 doi:10.1016/j.cell.2011.10.050
418 Insall, R.H., 2010. Understanding eukaryotic chemotaxis: a pseudopod-centred view. Nature
419 Publishing Group 11, 453–458. doi:10.1038/nrm2905

420 Kamon, H., Kawabe, T., Kitamura, H., Lee, J., Kamimura, D., Kaisho, T., Akira, S.,
421 Iwamatsu, A., Koga, H., Murakami, M., Hirano, T., 2006. TRIF-GEFH1-RhoB pathway is
422 involved in MHCII expression on dendritic cells that is critical for CD4 T-cell activation.
423 The EMBO Journal 25, 4108–4119. doi:10.1038/sj.emboj.7601286
424 Keren, K., Pincus, Z., Allen, G.M., Barnhart, E.L., Marriott, G., Mogilner, A., Theriot, J.A.,
425 2008. Mechanism of shape determination in motile cells. Nature 453, 475–U1.
426 doi:10.1038/nature06952
427 Krause, M., Gautreau, A., 2014. Steering cell migration: lamellipodium dynamics and the
428 regulation of directional persistence. Nature Publishing Group 15, 577–590.
429 doi:10.1038/nrm3861
430 Krendel, M., Zenke, F.T., Bokoch, G.M., 2002. Nucleotide exchange factor GEF-H1
431 mediates cross-talk between microtubules and the actin cytoskeleton. Nature Cell
432 Biology 4, 294–301. doi:10.1038/ncb773
433 Lämmermann, T., Bader, B.L., Monkley, S.J., Worbs, T., Wedlich-Söldner, R., Hirsch, K.,
434 Keller, M., Forster, R., Critchley, D.R., Fässler, R., Sixt, M., 2008. Rapid leukocyte
435 migration by integrin-independent flowing and squeezing. Nature 453, 51–55.
436 doi:10.1038/nature06887
437 Lämmermann, T., Renkawitz, J., Wu, X., Hirsch, K., Brakebusch, C., Sixt, M., 2009. Cdc42-
438 dependent leading edge coordination is essential for interstitial dendritic cell migration.
439 Blood 113, 5703–5710. doi:10.1182/blood-2008-11-191882
440 Leithner, A., Eichner, A., Müller, J., Reversat, A., Brown, M., Schwarz, J., Merrin, J., de
441 Gorter, D.J.J., Schur, F., Bayerl, J., de Vries, I., Wieser, S., Hauschild, R., Lai, F.P.L.,
442 Moser, M., Kerjaschki, D., Rottner, K., Small, J.V., Stradal, T.E.B., Sixt, M., 2016.
443 Diversified actin protrusions promote environmental exploration but are dispensable for
444 locomotion of leukocytes. Nature Cell Biology 18, 1253–1259. doi:10.1038/ncb3426
445 Lutz, M.B., Kukutsch, N., Ogilvie, A.L., Rössner, S., Koch, F., Romani, N., Schuler, G., 1999.
446 An advanced culture method for generating large quantities of highly pure dendritic cells
447 from mouse bone marrow. Journal of Immunological Methods 223, 77–92.
448 Matov, A., Applegate, K., Kumar, P., Thoma, C., Krek, W., Danuser, G., Wittmann, T., 2010.
449 Analysis of microtubule dynamic instability using a plus-end growth marker. Nat Meth 7,
450 761–768. doi:10.1038/nmeth.1493
451 Miller, A.L., Bement, W.M., 2009. Regulation of cytokinesis by Rho GTPase flux. Nature Cell
452 Biology 11, 71–U137. doi:10.1038/ncb1814
453 Mitchison, T., Kirschner, M., 1984. Dynamic instability of microtubule growth. Nature 312,
454 237–242.

455 Mitchison, T.J., Cramer, L.P., 1996. Actin-based cell motility and cell locomotion. Cell 84,
456 371–379.
457 Mogilner, A., Oster, G., 2003. Force generation by actin polymerization II: the elastic ratchet
458 and tethered filaments. Biophysj 84, 1591–1605. doi:10.1016/S0006-3495(03)74969-8
459 Murrell, M., Oakes, P.W., Lenz, M., Gardel, M.L., 2015. Forcing cells into shape: the
460 mechanics of actomyosin contractility. Nature Publishing Group 16, 486–498.
461 doi:10.1038/nrm4012
462 Niggli, V., 2003. Microtubule-disruption-induced and chemotactic-peptide-induced migration
463 of human neutrophils: implications for differential sets of signalling pathways. Journal of
464 Cell Science 116, 813–822. doi:10.1242/jcs.00306
465 Ohl, L., Mohaupt, M., Czeloth, N., Hintzen, G., Kiafard, Z., Zwirner, J., Blankenstein, T.,
466 Henning, G., Foerster, R., 2004. CCR7 governs skin dendritic cell migration under
467 inflammatory and steady-state conditions. Immunity 21, 279–288.
468 doi:10.1016/j.immuni.2004.06.014
469 Petrie, R.J., Yamada, K.M., 2012. At the leading edge of three-dimensional cell migration.
470 Journal of Cell Science 125, 5917–5926. doi:10.1242/jcs.093732
471 Redd, M.J., Kelly, G., Dunn, G., Way, M., Martin, P., 2006. Imaging macrophage chemotaxis
472 in vivo: studies of microtubule function in zebrafish wound inflammation. Cell Motil.
473 Cytoskeleton 63, 415–422. doi:10.1002/cm.20133
474 Redecke, V., Wu, R., Zhou, J., Finkelstein, D., Chaturvedi, V., High, A.A., cker, H.H.A.,
475 2013. Hematopoietic progenitor cell lines with myeloid and lymphoid potential. Nat Meth
476 1–13. doi:10.1038/nmeth.2510
477 Ren, Y., 1998. Cloning and Characterization of GEF-H1, a Microtubule-associated Guanine
478 Nucleotide Exchange Factor for Rac and Rho GTPases. Journal of Biological Chemistry
479 273, 34954–34960. doi:10.1074/jbc.273.52.34954
480 Renkawitz, J., Reversat, A., Leithner, A., Merrin, J., Sixt, M., 2018. Micro-engineered “pillar
481 forests” to study cell migration in complex but controlled 3D environments. Methods Cell
482 Biol. 147, 79–91. doi:10.1016/bs.mcb.2018.07.004
483 Renkawitz, J., Schumann, K., Weber, M., Lämmermann, T., Pflicke, H., Piel, M., Polleux, J.,
484 Spatz, J.P., Sixt, M., 2009. Adaptive force transmission in amoeboid cell migration.
485 Nature Cell Biology 11, 1438–1443. doi:10.1038/ncb1992
486 Renkawitz, J., Kopf, A., Stopp, J., de Vries, I., Driscoll M., Merrin, J., Hauschild, R., Welf, E.,
487 Danuser, G., Fiolka, R., Sixt, M., 2019. Nuclear positioning facilitates amoeboid
488 migration along the path of least resistance. Under revision.
489 Ridley, A.J., 2003. Cell Migration: Integrating Signals from Front to Back. Science 302,

1704–1709. doi:10.1126/science.1092053

Sanchez-Madrid, F., Del Pozo, M.A., 1999. Leukocyte polarization in cell migration and immune interactions. The EMBO Journal 18, 501–511. doi:10.1093/emboj/18.3.501

Shi, Z., Graber, Z.T., Baumgart, T., Stone, H.A., Cohen, A.E., 2018. Cell Membranes Resist Flow. Cell. doi:10.1016/j.cell.2018.09.054

Sixt, M., Lämmermann, T., 2011. In vitro analysis of chemotactic leukocyte migration in 3D environments. Methods Mol. Biol. 769, 149–165. doi:10.1007/978-1-61779-207-6_11

Stewart, S.A., Dykxhoorn, D.M., Palliser, D., Mizuno, H., Yu, E.Y., An, D.S., Sabatini, D.M., Chen, I., Hahn, W.C., Sharp, P.A., Weinberg, R.A., Novina, C.D., 2003. Lentivirus-delivered stable gene silencing by RNAi in primary cells. RNA 9, 493–501. doi:10.1261/rna.2192803

Takesono, A., Heasman, S.J., Wojciak-Stothard, B., Garg, R., Ridley, A.J., 2010. Microtubules Regulate Migratory Polarity through Rho/ROCK Signaling in T Cells. PLoS ONE 5, e8774–15. doi:10.1371/journal.pone.0008774

van Helvert, S., Storm, C., Friedl, P., 2018. Mechanoreciprocity in cell migration. Nature Cell Biology 20, 8–20. doi:10.1038/s41556-017-0012-0

Vargas, P., Barbier, L., Sáez, P.J., Piel, M., 2017. Mechanisms for fast cell migration in complex environments. Current Opinion in Cell Biology 48, 72–78. doi:10.1016/j.ceb.2017.04.007

Vicente-Manzanares, M., Sánchez-Madrid, F., 2004. Role of the cytoskeleton during leukocyte responses. Nat Rev Immunol 4, 110–122. doi:10.1038/nri1268

Waterman-Storer, C.M., Worthylake, R.A., Liu, B.P., Burridge, K., Salmon, E.D., 1999. Microtubule growth activates Rac1 to promote lamellipodial profusion in fibroblasts. Nature Cell Biology 1, 45–50. doi:10.1038/9018

Waterman-Storer, C.M., Salmon, E.D., 1997. Actomyosin-based retrograde flow of microtubules in the lamella of migrating epithelial cells influences microtubule dynamic instability and turnover and is associated with microtubule breakage and treadmilling. The Journal of Cell Biology 139, 417–434.

Weber, M., Hauschild, R., Schwarz, J., Moussion, C., de Vries, I., Legler, D.F., Luther, S.A., Bollenbach, T., Sixt, M., 2013. Interstitial Dendritic Cell Guidance by Haptotactic Chemokine Gradients. Science 339, 328–332. doi:10.1126/science.1228456

Weijer, C.J., 2009. Collective cell migration in development. Journal of Cell Science 122, 3215–3223. doi:10.1242/jcs.036517

Wittmann, T., Waterman-Storer, C.M., 2001. Cell motility: can Rho GTPases and microtubules point the way? Journal of Cell Science 114, 3795–3803.

525 Xu, J., Wang, F., Van Keymeulen, A., Rentel, M., Bourne, H.R., 2005. Neutrophil
526 microtubules suppress polarity and enhance directional migration. Proc. Natl. Acad. Sci.
527 U.S.A. 102, 6884–6889. doi:10.1073/pnas.0502106102
528 Yoo, S.K., Lam, P.-Y., Eichelberg, M.R., Zasadil, L., Bement, W.M., Huttenlocher, A., 2012.
529 The role of microtubules in neutrophil polarity and migration in live zebrafish. Journal of
530 Cell Science 125, 5702–5710. doi:10.1242/jcs.108324
531

532 **Figure legends**

533 **Figure 1. Microtubules control dendritic cell polarity.**

534 **(A)** *In situ* migration of endogenous DCs on a mouse ear sheet. Z-projections of separated
535 ear sheets upon control conditions (DMSO) or pharmacological treatment (Nocodazole).
536 Lymphatic vessels were stained for Lyve-1, DCs for MHC-II. Mean distance from lymphatic
537 vessels of endogenous DCs was determined 48h after ear separation (lower panel). Per
538 condition, four mouse ears with two fields of view were analyzed. Boxes extend from 25th to
539 75th percentile. Whiskers span minimum to maximum values. ** $P \leq 0.01$. Scale bar, 100μm.
540 **(B)** Automated analysis of y-directed migration speed within three-dimensional collagen
541 network along soluble CCL19 gradient. Plot shows mean migration velocities over time ±
542 S.D. from 4 experiments. Directionality during **(C)** three-dimensional (n = 50 cells per
543 condition, N = 3 experiments)**, (D)** two-dimensional (n = 50 cells per condition, N = 4
544 experiments) and **(J)** one-dimensional (n = minimum of 64 cells per condition, N = 3
545 experiments) migration was assessed by comparing accumulated- with euclidean-distance
546 of manually tracked cell trajectories. Boxes extend from 25th to 75th percentile. Whiskers
547 span minimum to maximum values **** $P \leq 0.0001$ **(E)** Individual cell migration trajectories
548 within two-dimensional confinement upon control (DMSO) and pharmacological
549 (Nocodazole) treatment of n = 58 cells (DMSO) and n = 52 cells (Noco.) from N = 4
550 experiments. **(F)** Individual cell outlines over time upon control or Nocodazole-treated
551 conditions. **(G)** Migration speed within two-dimensional confinement along soluble CCL19
552 gradient upon control (DMSO) and pharmacological (Nocodazole) treatment of n = 50 cells
553 per condition from N = 4 experiments. Boxes extend from 25th to 75th percentile. Whiskers
554 span minimum to maximum values. **(H)** Time-lapse sequence of control or Nocodazole-
555 treated DCs migrating within a one-dimensional microchannel showing oscillatory migration
556 behavior upon Nocodazole-treatment. **(I)** Migration velocities of control or Nocodazole-
557 treated DCs migrating within a one-dimensional microchannel of n = minimum of 64 cells per
558 condition from N = 3 experiments. Boxes extend from 25th to 75th percentile. Whiskers span
559 minimum to maximum values. ** $P \leq 0.01$. See also Figure S1.

560

561

562 **Figure 2. Microtubules control polar cellular organization via the contractile module.**

563 **(A)** Levels of active RhoA upon MT disruption with Nocodazole determined by luminometry.
564 RhoA activity levels were normalized to Nocodazole treated samples. Plotted is mean ± S.D.
565 from N = 3 experiments. **** $P \leq 0.0001$. **(B)** Levels of MLC phosphorylation by Western Blot
566 analysis. Cells were pretreated with the indicated compounds (DMSO, CCL19, CCL21,

567 Nocodazole, Y27632 together with Nocodazole (Y/N)). Mean fluorescence intensity of pMLC
568 was normalized to GAPDH signal and shown as fold increase relative to DMSO control ±
569 S.D. Blots are representative of N = 3 experiments. ** P ≤ 0.01. **(C)** DCs migrating within a
570 collagen gel either non-treated (NT) or double-treated with Y27632 and Nocodazole (Y/N).
571 Note the different time intervals per condition. **(D)** Automated analysis of y-directed speed of
572 non-treated, Nocodazole-treated (Noc.) or double-treated cells using Y27632 and
573 Nocodazole (Y/N). Plot shows mean migration velocities over time ± S.D. from N = 4
574 experiments. **(E)** Morphologies of non-treated (NT), Nocodazole- (Noco.) treated and
575 double-treated (Y/N) cells using Y27632 and Nocodazole migrating under agarose. **(F)**
576 Directionalities of non-treated (NT), Nocodazole- (Noco.) treated and double-treated cells
577 using Y27632 and Nocodazole (Y/N) of n = 25 cells per condition from N = 3 experiments.
578 Boxes extend from 25th to 75th percentile. Whiskers span minimum to maximum values. ****
579 P ≤ 0.0001. **(G)** Migration velocities within two-dimensional confinement along soluble
580 CCL19 gradient upon control (DMSO), Nocodazole- (Noc) and double-treatment (Y/N) with
581 Y27632 and Nocodazole (n = 25 cells per condition from N = 3 experiments). Boxes extend
582 from 25th to 75th percentile. Whiskers span minimum to maximum values. **** P ≤ 0.0001.
583 **(H)** Time-lapse sequence of non-treated (NT) or double-treated cells using Y27632 and
584 Nocodazole (Y/N) DCs migrating within microchannels. **(I)** Directionalities of non-treated
585 (NT), Nocodazole- (Noc.) treated or double-treated (Y/N) cells using Y27632 and
586 Nocodazole within microchannels (n = minimum of 74 cells per condition from N = 4
587 experiments). Boxes extend from 25th to 75th percentile. Whiskers span minimum to
588 maximum values. *** P ≤ 0.001, **** P ≤ 0.0001. **(J)** Migration velocities of non-treated (NT),
589 Nocodazole- (Noc.) treated or double-treated (Y/N) cells using Y27632 and Nocodazole
590 within microchannels (n = minimum of 74 cells per condition from N = 4 experiments). Boxes
591 extend from 25th to 75th percentile. Whiskers span minimum to maximum values. **** P ≤
592 0.0001.
593
594 **Figure 3. Polarized microtubule dynamics locally activate the contractile module.**
595 Cells migrating under agarose along a soluble CCL19 gradient were fixed and stained for
596 alpha-Tubulin and the nucleus (DAPI). Boxed regions indicate trailing edge (purple) or
597 pioneering (gray) MTs towards the leading edge. Scale bar, 10μm. Right panel: Line scan of
598 alpha-tubulin distribution along the anterior-posterior polarization axis, derived from purple
599 line in left panel. Scale bar, 10μm. **(B)** Determination of MTOC position by alpha- and
600 gamma-tubulin staining with respect to the nucleus. Mean ± S.D. of n = 256 cells from N = 3
601 experiments. **(C)** Angular distribution of automatically detected MT growth events along

602 anterior-posterior polarization axis. **(D)** MT dynamics during directed migration. Growth and
603 shrinkage frequencies of individual MT filaments (EMTB) were assessed in protrusive (front,
604 grey box) vs. contractile (back, purple box) areas of the same migratory cell. Growth events
605 and catastrophes ≥1μm were tracked for n = 10 filaments in the respective region of N = 8
606 cells. Mean ± S.D. **** P ≤ 0.0001. Scale bar, 5μm. **(E)** Acetylated MTs in DCs fixed while
607 migrating under agarose. Levels of acetylation were assessed by measuring mean
608 fluorescence intensity of acetylated Tubulin along individual alpha-Tubulin filaments of (n =
609 87 filaments per condition of N = 3 experiments) directed towards the front (gray) or back
610 (purple). Boxes extend from 25th to 75th percentile. Whiskers span minimum to maximum
611 values. **** P ≤ 0.0001. Scale bar, 10μm. **(F)** EB3-mCherry localization of control or PST-1
612 treated cells migrating under agarose. The red box indicates photo-activated area magnified
613 below. Magnified regions show EB3-mCherry intensities after local photo-activation. Lower
614 panel indicates fluorescence intensity evolution upon photo-activation of control or PST-1
615 treated cells. The red line highlights the time point of initial photo-activation. **(G)** Time-lapse
616 sequence of control or PST-1 treated cells, which were locally photo-activated (red box)
617 during migration under agarose. **(H)** Kymograph analysis of the photo-activated area of **(G)**.
618 The time point of local photo-activation is shown in red. Right panel: Frequency of local
619 retractions upon photo-activation of control or PST-1 treated DCs during migration (n = 26
620 cells per condition ± S.D. from N = 3 experiments). * P ≤ 0.05, **** P ≤ 0.0001. See also
621 Figure S2.
622
623 **Figure 4. Accumulation of Lfc precedes cellular retraction**
624 **(A)** Polarized distribution of Lfc-GFP during DC migration. Shown is a maximum intensity
625 time projection of a double-fluorescent reporter cell expressing Lfc-GFP and EB3-mCherry
626 over 8.5min. Diffuse Lfc-GFP accumulation is highlighted in the trailing edge (purple
627 arrowhead) and in retracting protrusions (orange arrowhead). Scale bar, 10μm. **(B)**
628 Enrichment of non-filamentous Lfc-GFP or EB3-mCherry signal in the rear versus the front
629 of migrating cells. Shown is a maximum intensity time projection over 100sec. Scale bar,
630 5μm. Lower panel: Relative enrichment of non-filamentous fluorescence signal intensities of
631 Lfc-GFP and EB3-mCherry in rear versus the front of n = 16 cells per condition from N = 3
632 experiments. Boxes extend from 25th to 75th percentile. Whiskers span minimum to
633 maximum values. **** P ≤ 0.0001. **(C)** Localization of Lfc-GFP and MLC-RFP in protrusive
634 (front, gray box) or contractile (back, purple box) areas. Correlation of co-localization
635 between Lfc-GFP and MLC-RFP. Hot colors in right image indicate strong co-localization of
636 both signals, cold colors specify exclusion. Co-localization was determined separately in

637 actively protruding (grey box) and retracting (purple box) areas in migrating cells. Boxed
638 regions indicate exemplary regions used for analysis of n = 8 cells ± S.D. Scale bar, 10μm.
639 **(D)** Distribution of Lfc-GFP and MLC-RFP during a protrusion-retraction cycle. Time course
640 of protrusion-formation and protrusion-retraction of a migrating double fluorescent reporter
641 cell expressing Lfc-GFP and MLC-RFP. Lower panel represents fluorescence intensity
642 evolution during the entire protrusion-retraction cycle. Scale bar 5 μm. **(E)** Accumulation of
643 Lfc-GFP precedes retraction of explorative protrusions (orange arrowheads). Time-lapse
644 sequence of an explorative protrusion-retraction cycle of a cell migrating within a complex
645 three-dimensional pillar forest. Scale bar 10 μm. Right panel represents time projection over
646 16 minutes, showing Lfc accumulation in explorative protrusion (orange arrowhead) while
647 maintaining a straight migration path according do EB3-mCherry signal distribution (lower
648 panel).
649
650 **Figure 5. Lfc specifies myosin localization at the trailing edge.**
651 **(A)** Myosin light chain-GFP expressing DC migrating under agarose along a soluble CCL19
652 gradient. Central (orange box) and uropodal (purple box) MLC accumulation is outlined.
653 Scale bar, 10μm. **(B)** Left panel: Scheme of quantifying relative position of MLC
654 accumulation during directed cell migration. Right panel: Position of MLC accumulation in
655 relation to migration speed. MLC accumulation under **(C)** untreated**, (D)** Nocodazole-treated
656 or **(E)** *lfc*-deficient conditions. Scale bar 10μm. Middle panels indicate cell shapes over time.
657 Right panels indicate mean MLC fluorescence distribution along the anterior-posterior
658 polarization axis (dashed line) in 80sec intervals. **(F)** Quantification according to **(B)** showing
659 MLC accumulation during directed migration of $lfc^{+/+}$ (red) and $lfc^{-/-}$ (blue) DCs. To account
660 for differences in cell length the distance between cell center and MLC accumulation was
661 normalized to cell length. Graph shows distance of n = 7 migratory cells per condition ± S.D.
662 **(G)** Localization of endogenous phospho-MLC(S19) in fixed migratory DCs. Right panel
663 indicates position of MLC accumulation relative to cell length of n = 16 cells per condition
664 from N = 4 experiments. Boxes extend from 25th to 75th percentile. Whiskers span minimum
665 to maximum values. **** $P \leq 0.0001$. Scale bar 10μm. **(H)** Localization of Moesin in fixed
666 migratory $lfc^{+/+}$ (red) and $lfc^{-/-}$ (blue) DCs. Right panel: Quantification of fluorescence intensity
667 in leading versus trailing edge regions of $lfc^{+/+}$ (red) and $lfc^{-/-}$ (blue) DCs of n = 55 cells per
668 condition from N = 3 experiments. Boxes extend from 25th to 75th percentile. Whiskers span
669 minimum to maximum values. *** $P \leq 0.001$, **** $P \leq 0.0001$. Scale bar 10μm. **(I)** Western
670 Blot analysis of $lfc^{+/+}$ and $lfc^{-/-}$ DCs for phospho-ERM protein levels. Right panel:
671 Quantification of pERM levels upon treatment with DMSO, CCL19, Nocodazole or Y27632.

672 Right panel: Increase in signal intensity relative to *lfc*$^{+/+}$ control (DMSO) conditions. Mean
673 fluorescence intensity of pERM signal was normalized to total ERM signal and shown as fold
674 increase relative to *lfc*$^{+/+}$ DMSO control ± S.D. of N = 3 experiments. See also Figure S3.
675
676 **Figure 6. Lfc controls DC migration by regulating MT mediated adhesion resolution.**
677 **(A)** *In situ* migration of exogenous DCs on a mouse ear sheet. Lymphatic vessels were
678 stained for Lyve-1, DCs with TAMRA respectively. Right panel indicates the mean distance
679 of cells from lymphatic vessels. Per experiment two mouse ears with two fields of view were
680 analyzed of N = 4 experiments. Boxes extend from 25th to 75th percentile. Whiskers span
681 minimum to maximum values. * P ≤ 0.05. Scale bar, 100μm. **(B)** Automated analysis of y-
682 directed migration speed within a collagen network along soluble CCL19 gradient. Cells
683 were either non-treated or treated with Y27632. Plot shows mean migration velocities over
684 time ± S.D. from N = 7 experiments. **(C)** Cell outlines of *lfc*$^{+/+}$ (red) and *lfc*$^{-/-}$ (blue) DCs
685 migrating within a collagen network along a soluble CCL19 gradient. Scale bar, 10μm. **(D)**
686 Lengths of cells migrating within a collagen network of n = 85 individual cells per condition
687 from N = 4 experiments. Boxes extend from 25th to 75th percentile. Whiskers span minimum
688 to maximum values. *** P ≤ 0.001. **(E)** Cell outlines of *lfc*$^{+/+}$ and *lfc*$^{-/-}$ DCs migrating under
689 agarose under adhesive conditions (FCS). Cells were either non-treated (NT) or treated with
690 Nocodazole (Noc.) Lower panel: Cell lengths of n = minimum of 80 cells per condition from N
691 = 5 experiments. Boxes extend from 25th to 75th percentile. Whiskers span minimum to
692 maximum values. **** P ≤ 0.0001. Scale bar, 10μm. **(F)** Cell outlines of *lfc*$^{+/+}$ and *lfc*$^{-/-}$ DCs
693 migrating under agarose under non-adhesive conditions (PEG). Cells were either non-
694 treated (NT) or treated with Nocodazole (Noc.) Lower panel: Cell lengths of n = minimum of
695 80 cells per condition from N = 5 experiments. Boxes extend from 25th to 75th percentile.
696 Whiskers span minimum to maximum values. **** P ≤ 0.0001. Scale bar, 10μm. **(G)**
697 Migration distance of *lfc*$^{+/+}$ and *lfc*$^{-/-}$ DCs migrating under agarose under non-adhesive
698 conditions (PEG) of n = minimum of 80 cells per condition from N = 5 experiments. Cells
699 were either non-treated (NT) or treated with Nocodazole (Noc.). Boxes extend from 25th to
700 75th percentile. Whiskers span minimum to maximum values. * P ≤ 0.05, **** P ≤ 0.0001. **(H)**
701 Directionality of *lfc*$^{+/+}$ and *lfc*$^{-/-}$ DCs migrating under agarose under non-adhesive conditions
702 (PEG). Cells were either non-treated (NT) or treated Nocodazole (Noc.) of n = minimum of
703 80 cells per condition from N = 5 experiments. Boxes extend from 25th to 75th percentile.
704 Whiskers span minimum to maximum values. **** P ≤ 0.0001. See also Figure S4.
705
706

Figure 7. Microtubules mediate retraction of supernumerary protrusions via Lfc.

(A) Migration within a microchannel path choice assay. Graphs shows junction point passing times of *lfc*$^{+/+}$ (n = 79 cells of N = 3 experiments) and *lfc*$^{-/-}$ (n = 49 cells of N = 2 experiments) DCs. Boxes extend from 25th to 75th percentile. Whiskers span minimum to maximum values. *** P ≤ 0.001. **(B)** Junction point passing times depending on presence of non-competing or multiple competing protrusions per cell of *lfc*$^{+/+}$ (n = 37 cells of N = 3 experiments) and *lfc*$^{-/-}$ (n = 46 cells of N = 2 experiments) DCs. Boxes extend from 25th to 75th percentile. Whiskers span minimum to maximum values. ** P ≤ 0.01. **(C)** Time-lapse sequence of *lfc*$^{+/+}$ and *lfc*$^{-/-}$ DCs migrating within a path choice assay. White arrowheads in lower panel highlight cell rupturing events. **(D)** Frequency of cell rupturing events during path-choice decision of *lfc*$^{+/+}$ (n = 79 cells ± S.D. of N = 3 experiments) and *lfc*$^{-/-}$ (n = 52 cells ± S.D. of N = 2 experiments) DCs. **(E)** Migration of DCs within straight constriction-containing microchannels. Graphs shows constriction point passing times of *lfc*$^{+/+}$ (n = 114 cells of N = 3 experiments) and *lfc*$^{-/-}$ (n = 195 cells of N = 3 experiments) DCs. Boxes extend from 25th to 75th percentile. Whiskers span minimum to maximum values. **(F)** Time-lapse sequence of *lfc*$^{+/+}$ and *lfc*$^{-/-}$ DCs migrating within straight microchannels. **(G)** Directionality of cell trajectories within straight microchannels of n = minimum of 80 cells per condition from N = 5 experiments. Boxes extend from 25th to 75th percentile. Whiskers span minimum to maximum values. * P ≤ 0.05, ** P ≤ 0.01, *** P ≤ 0.001, **** P ≤ 0.0001. **(H)** Migration speed of *lfc*$^{+/+}$ and *lfc*$^{-/-}$ DCs within straight microchannels of n = minimum of 80 cells per condition from N = 5 experiments. Boxes extend from 25th to 75th percentile. Whiskers span minimum to maximum values. *** P ≤ 0.001.

730 **Materials and Methods**

731 **Generation of Lfc-deficient mice**

732 A cosmid containing the full genomic sequence of the gene that encodes Lfc (*Arhgef2*) was
733 isolated from a 129 mouse genomic library with Lfc cDNA probes (106-630, 631-1057 and
734 1060-1478 bp) amplified by RT-PCR. The genomic DNA region between base pairs 1193-
735 1477, coding for amino acids 351-445 in the DH domain and DH/PH domain interface was
736 exchanged for a neomycin cassette flanked by LoxP sites. The targeting construct was
737 linearized with *Not*I and electroporated into R1 ES cells. Homologous recombinants were
738 selected in the presence of G418 (150 μg/ml) and gancyclovir (2 μM) and analyzed by
739 Southern blotting. Positive embryonic stem cell clones were aggregated with eight cell-stage
740 mouse embryos to generate chimeras. The resulting mice were genotyped by Southern blot
741 and PCR. Primers (5′– CGGGGATCCATTCGGTTGTAA –3′) and (5′–
742 AAGCGGCATGGAGTTCAGGA –3′) amplified a 365-bp fragment specific for the wild type
743 allele, whereas primers (5′– AGAGTTCTGCAGCCGCCACACCA–3′) and 5′–
744 GGTGGGGGTGGGGTGGGATTAGATA –3′) amplified a 500-bp fragment specific for the
745 targeted allele. We refer to these mice as *lfc*$^{-/-}$ mice throughout the entire manuscript.
746 Western blot analysis using a Lfc-specific antibody was performed to confirm that *lfc*$^{-/-}$ mice
747 had no expression of Lfc protein. Mice were backcrossed to C57Bl/6 background for more
748 than 12 generations. Dendritic cells were generated from bone marrow isolated from
749 littermates or age-matched wildtype and *lfc*-deficient 8-12 week-old mice. Mice were bred
750 and housed in accordance with institutional guidelines.

751

752 **Generation of immortalized hematopoietic progenitor reporter cell lines**

753 Hematopoietic progenitor cell lines were generated by retroviral delivery of an estrogen-
754 regulated form of HoxB8 as described recently (Redecke et al., 2013). Briefly, bone marrow
755 of 6-12 week of *lfc*$^{+/+}$ and *lfc*$^{-/-}$ mice was isolated and retrovirally transduced with an
756 estrogen-regulated form of the HoxB8 transcription factor. After expansion of immortalized
757 cells, lentiviral spin infection (1500g, 1h) was carried out in the presence of 8μg/ml
758 Polybrene and the lentivirus coding for fluorescent expression construct of interest.
759 Following transduction, cells were selected for stable virus insertion using 10μg/ml
760 Blasticidin for at least one week. Cells expressing fluorescent reporter constructs were
761 sorted using fluorescence-activated cell sorting (FACS Aria III, BD Biosciences) prior to
762 migration experiments.

763

764

765 **Dendritic cell culture**

766 Culture was started either from freshly isolated bone marrow of 6-12 week old mice as
767 described earlier (Lutz et al., 1999) or from stable hematopoietic progenitor cell lines after
768 washing out estrogen. DC differentiation was induced by plating $2x10^6$ cells (bone marrow)
769 or $2x10^5$ cells (progenitor cells) in complete media (RPMI 1640 supplemented with 10%
770 Fetal Calf Serum, 2mM L-Glutamine, 100U/ml Penicillin, 100μg/ml Streptomycin, 50μM ß-
771 Mercaptoethanol) (all purchased from Invitrogen) containing 10% Granulocyte-Monocyte
772 colony stimulating factor (GM-CSF, supernatant from hybridoma culture). To induce
773 maturation, cells were stimulated overnight with 200ng/ml Lipopolysaccharide from *E.coli*
774 0127:B8 (Sigma) and used for experiments on days 9-10.

775

776 ***In situ* migration assay**

777 Six to eight weeks old female C57BL/6J mice were sacrificed and individual ear sheets
778 separated into dorsal and ventral halves. *Endogenous cell migration:* Cartilage free ventral
779 halves were incubated for 48h at 37˚C, 5% CO_2 with ventral side facing down in a well plate
780 filled with complete medium. The medium was changed once 24h post-incubation-start. If
781 indicated, pharmacological inhibitors were added to the medium. Ear sheets were fixed with
782 1% PFA followed by immersion in 0.2% Triton X-100 in PBS for 15min and three washing
783 steps á 10min with PBS. Unspecific binding was prevented by 60min incubation in 1%BSA
784 in PBS at room temperature. Incubation with primary rat-polyclonal antibody against LYVE-1
785 in combination with rat-polyclonal biotinylated anti-MHC-II antibody (both R&D Systems) was
786 done for 2h at room temperature. After three times 10min washing with 1% BSA in PBS
787 consecutive incubation using Alexa Fluor 488-AffiniPure $F(ab')_2$ fragment donkey anti-rat IgG
788 (H+L) secondary antibody and streptavidin-Cy3 secondary antibody (both Jackson Immuno)
789 was done. Samples were incubated 45min in first secondary antibody in the dark followed by
790 10min washing in 1% BSA in PBS and subsequent incubation with second secondary
791 antibody. Samples mounted with ventral side up on a microscope slide, protected with a
792 coverslip and stored at 4˚C in the dark. *Exogenous cell migration:* Cartilage free ventral ear
793 halves were mounted on a plastic ring, followed by application of $1x10^5$ exogenously
794 differentiated DCs stained with 7μM TAMRA (Invitrogen). If indicated, cells were pretreated
795 with pharmacological inhibitors. Cells were allowed to migrate into the tissue for 20min
796 followed by three washing steps using complete media. Subsequently, ears were incubated
797 in complete media for 45min at 37˚C, 5% CO_2 before continuing with fixation and
798 immunostaining procedure (see above).

799 In order to determine the distance between the lymphatic vessels and DCs a mask was
800 created by manually outlining lymphatic vessels depending on Lyve-1 staining and
801 segmenting cells according to their fluorescence intensity. The distance between cells and
802 lymphatic vessels was quantified using a custom-made Matlab script, which determines the
803 closest distance from the segmented cells to the border of the lymphatic vessel binary
804 image. Image borders were excluded from analysis.
805
806 ***In vitro* collagen gel migration assay**
807 Custom made migration chambers were assembled by using a plastic dish containing a
808 17mm hole in the middle, which was covered by coverslips on each side of the hole. Three-
809 dimensional scaffolds consisting of 1.73mg/ml bovine Collagen I were reconstituted *in vitro*
810 by mixing $3x10^5$ cells in suspension with Collagen I suspension buffered to physiological pH
811 with Minimum Essential Medium and Sodium Bicarbonate in a 1:2 ratio. To allow
812 polymerization of Collagen fibers, gels were incubated 1h at 37˚C, 5% CO_2. Directional cell
813 migration was induced by overlaying the polymerized gels with 0.63μg/ml CCL19 diluted in
814 complete media (R&D Systems). To prevent drying-out of the gels, migration chambers were
815 sealed with Paraplast X-tra (Sigma-Aldrich). The acquisition was performed in 60sec
816 intervals for five hours at 37˚C, 5% CO_2. Detailed description of experimental procedure can
817 be found elsewhere (Sixt and Lämmermann, 2011).
818
819 **Analysis of y-displacement**
820 Quantification of y-directed migration analysis of cell population was performed as described
821 earlier (Leithner et al., 2016). Briefly, raw data image sequences were background corrected
822 and particles smaller and bigger than an average cell were excluded. For each time point the
823 lateral displacement in y-direction was determined with the previous frame to generate the
824 best overlap, which yields the y-directed migration velocity of a cell population.
825
826 **Migration within micro-fabricated polydimethylsiloxane (PDMS) based devices.**
827 Generation of PDMS-based devices and detailed experimental protocols can be found
828 elsewhere (Leithner et al., 2016). Briefly, photomasks were designed using Coreldraw X18,
829 printed on a photomask (5" square quartz, 1μm resolution, JD Photo data), followed by a
830 spin coating step using SU-8 2005 (3000 RPM, 30sec, Microchem, USA) and a prebake of 2
831 min at 95˚C. The wafer was then exposed to ultra-violet light (90 – 105 mJ/cm^2 on an EVG
832 mask aligner). After a post-exposure bake of 3 min 95˚C, the wafer was developed in
833 PGMEA. A one-hour silanization with Trichloro(1H,1H,2H,2H-perfluorooctyl)silane was

834 applied to the wafer. The devices were made with a 1:10 mixture of Sylgard 184 (Dow
835 Corning). Air bubbles were removed with a desiccator. The PDMS was cured overnight at
836 85˚C. Micro-devices were attached to ethanol cleaned coverslips after plasma cleaning for
837 1h at 85˚C.
838
839 ***In vitro* under-agarose migration assay**
840 To obtain humid migration chambers a 17mm plastic ring was attached to a glass bottom
841 dish using Paraplast X-tra (Sigma-Aldrich) to seal attachment site. For under-agarose
842 migration assay, 4% Ultra Pure Agarose (Invitrogen) in nuclease-free water (Gibco) was
843 mixed with phenol-free RPMI-1640 (Gibco) supplemented with 20% FCS, 1x Hanks buffered
844 salt solution pH 7.3 in a 1:3 ratio. Ascorbic acid was added to final concentration of 50μM
845 and a total volume of 500μl agarose-mix was cast into each migration chamber. After
846 polymerization, a 2mm hole was punched into the agarose pad and 2.5μg/ml CCL19 (R&D
847 Systems) was placed into the hole to generate a soluble chemokine gradient. Outer parts of
848 the dish were filled with water followed by 30-minute equilibration at 37˚C, 5% CO_2. The cell
849 suspension was injected under agarose opposite of the chemokine hole to confine DCs
850 between coverslip and agarose. Prior to acquisition, dishes were incubated at least two
851 hours at 37˚C, 5% CO_2 to allow recovery and persistent migration of cells. During
852 acquisition, dishes were held under physiological conditions at 37˚C and 5% CO_2.
853
854 **Immunofluorescence**
855 For fixation experiments a round shaped coverslip was placed in glass bottom dish before
856 casting of agarose and injection of cells. Migrating cells were fixed by adding prewarmed 4%
857 Para-Formaldehyde (PFA) diluted in cytoskeleton Buffer pH6.1 (10mM MES, 150mM NaCl,
858 5mM EGTA, 5mM Glucose, 5mM $MgCl_2$) directly on top of the agarose. After fixation,
859 agarose pad was carefully removed using a coverslip-tweezer followed by 20min incubation
860 of the coverslip in 0.5% Triton X-100 in PBS and three subsequent washing steps á 10min
861 with Tris-buffered saline (TBS) containing 0.1% Tween-20 (Sigma). Samples were blocked
862 to prevent unspecific binding by incubating 60min in blocking solution (5% BSA, 0.1%
863 Tween-20 in TBS). Immunostainings were carried out consecutively by 2h incubation with rat
864 monoclonal anti-alpha-tubulin (AbD serotec), mouse anti-phospho-Myosin light chain 2 (S19)
865 (Cell signaling), mouse anti-gamma tubulin (Sigma) or rabbit anti-acetylated alpha-tubulin
866 (Sigma). Followed by 3x10min washing with blocking solution and 30min incubation using
867 Alexa Fluor® 488-AffiniPure $F(ab')_2$ or Alexa Fluor® 647-AffiniPure $F(ab')_2$ Fragment IgG
868 (H+L) (both Jackson Immuno) secondary antibodies. After incubation washing was done at

869 least three times á 5min. Samples were conserved in non-hardening mounting medium with
870 DAPI (VectorLaboratories) and stored at 4˚C in the dark.
871
872 **Immunodetection of whole cell lysates**
873 $3x10^5$ cells were serum starved for 1h followed by drug treatment. After harvesting, cell
874 pellet was snap frozen and lysed using RIPA buffer (Cell Signaling) to which 1mM
875 Phenylmethylsulfonylfluoride was added prior to usage. Samples were supplemented with
876 LDS Sample Buffer and Reducing agent (both Invitrogen) and incubated for 5min at 90˚C
877 before loading on pre-cast 4-12% Bis-Tris acrylamide gel (Invitrogen). Subsequently,
878 samples were transferred to Nitrocellulose membrane using iBlot system (Invitrogen) and
879 blocked for 1h in 5% bovine serum albumin in TBS containing 0.01% Tween-20. For whole
880 cell lysate protein detection following antibodies were used: rabbit anti phospho-Myosin Light
881 Chain 2 (S19) (1:500), rabbit anti Myosin Light Chain 2 (1:500), rabbit anti GEF-H1 (the
882 mammalian homologue of Lfc) (1:500), rabbit anti phospho-ERM (1:500), rabbit anti ERM
883 (1:500, all Cell Signaling), mouse anti glyceraldehyde 3-phosphate dehydrogenase
884 (GAPDH) (1:1000, BioRad). As secondary antibodies Horseradish Peroxidase (HRP)
885 Conjugated Anti-rabbit and anti-mouse IgG (H + L) antibodies were used in 1:5000 dilutions
886 and enzymatic reaction was started by addition of chemoluminescent substrate for HRP
887 (Super Signal West Femto). Chemoluminescence was acquired using a VersaDoc imaging
888 system (BioRad). Western blot signals were quantified manually by normalization to input
889 values and subsequent comparison of each treatment to signal intensity of steady-state level
890 (i.e. control sample).
891
892 **Flow cytometry**
893 Before staining, $1\text{-}2x10^6$ cells were incubated for 15 min at +4°C with blocking buffer
894 (1xPBS, 1% BSA, 2mM EDTA) containing 5mg/ml α-CD16/CD32 (2.4G2, BD Biosciences).
895 For surface staining, cells were incubated for 30 min at 37°C with conjugated monoclonal
896 antibodies (mAbs; mouse α-CCR7-PE (4B12), rat α-mouse I-A/I-E-eFluor450 (M5/114.15.2),
897 hamster α-mouse CD11c-APC (N418)) diluted at the recommended concentration in
898 blocking buffer. Flow cytometry analysis was performed on a FACS CANTO II flow
899 cytometer (BD Biosciences).
900
901 **Pharmacological inhibitors**
902 For perturbation of cytoskeletal and myosin dynamics we used final concentrations of 300nM
903 Nocodazole and 10μM Y27632 (all purchased from Sigma Aldrich). Nocodazole was

904 dissolved in dimethylsulfoxide (DMSO) and Y27632 in poly-buffered saline. Control samples
905 were usually treated with 1:1000 DMSO if not indicated differentially.
906
907 **Fluorescent reporter constructs**
908 Generation of a C-terminal eGFP fusion construct of Lfc was carried out by amplifying Lfc
909 from DC cDNA using a NotI restriction site containing forward (5'
910 ATATGCGGCCGCAATCTCGGATCGAATCCCTCACTCGCG 3') and reverse (5'
911 ATATGCGGCCGCTTAGCTCTCTGAAGCTGTGGGCTCC 3') primer pair. After NotI
912 digestion, Lfc was cloned into a pcDNA3.1 backbone containing eGFP (Express Link™ T4
913 DNA-Ligase). Correct sequence and orientation of clones was verified by sequencing
914 (Eurofins). The fluorescent plasmid DNA reporter construct coding for EB3-GFP was a kind
915 gift of V. Small (IMBA, Austria). M. Olson (Beatson Institute) generously provided MLC
916 constructs (either fused to eGFP or RFP) (Croft et al., 2005) and EMTB-3xmCherry
917 constructs were a kind gift of (W. M. Bement, University of Wisconsin) (Miller and Bement,
918 2009). Gateway cloning technology™ was employed to generate lentivirus from plasmid
919 DNA constructs. Briefly, corresponding DNA segments were amplified using primers
920 containing overhangs with *att*B1 and *att*B2 recombination sites on the 3'- and the 5'-end
921 respectively. In order to obtain an EMTB fusion construct carrying a single mCherry tag, the
922 PCR product was size separated via gel electrophoresis and only the fragment of
923 corresponding size (EMTB: 816bp, mCherry: 705bp) was further processed. Gel purified
924 PCR fragments were inserted into pcDNA221 entry vectors (Invitrogen) via BP
925 recombination reaction, generating the entry clone. Expression clones were obtained by
926 carrying out the LR recombination reaction between entry clone and pLenti6.3 destination
927 vector (Invitrogen). Lentivirus production was carried out by co-transfecting LX-293 cells
928 (Chemicon) with the expression clone of interest in conjunction with pdelta8.9 (packaging
929 plasmid) and pCMV-VSV-G (envelope plasmid) (plasmids were a gift from Bob Weinberg)
930 (Stewart et al., 2003). The supernatant of virus-producing cells was harvested 72h after
931 transfection, snap frozen and stored at -80˚C after sterile filtration.
932
933 **Transgene delivery**
934 To induce expression of fluorescently labeled proteins DCs were transfected according to
935 manufacturer guidelines using nucleofector kit for primary T cells (Amaxa, Lonza Group).
936 Briefly, $5x10^6$ were resuspended in 100μl reconstituted nucleofector solution, transferred to
937 an electroporation cuvette and a total amount of 4μg plasmid DNA was added. Cells were
938 transfected by using a protocol specifically designed for electroporating immature mouse

939 DCs (program X-001). After transfection, cells were cultured in 60mm cell culture dishes in
940 complete media and taken for experiments 24h post-transfection. Due to low transfection
941 efficiency of primary cells, transfected cells were FACS sorted prior to experiment using
942 FACS Aria III (BD Biosciences).
943
944 **Luminometric RhoA activity assay**
945 RhoA activities were determined using G-LISA™ RhoA Activation Assay Biochem Kit™
946 (Cytoskeleton) according to the manufacturer's instructions. Briefly, $4x10^5$ mature BMDCs
947 were lysed in 70µl RIPA buffer (Cell Signaling) and protein concentration determined using
948 the Precision Red™ Advanced Protein Assay Reagent (Cytoskeleton). Respective samples
949 were treated with 300nM Nocodazole for 15 min before lysis. All samples were adjusted to a
950 final protein concentration of 0.5mg/ml. Luminescence signals were measured using a
951 microplate photometer at 600nm. Wells containing lysis buffer only were used as reference
952 blanks in all experiments.
953
954 **Microscopy**
955 Low magnification bright field or DIC time-lapse acquisition was carried out using inverted
956 routine microscopes (Leica), equipped with PAL cameras (Prosilica, Brunaby, BC) controlled
957 by SVS-Visitek software (Seefeld, Germany). Acquisition was conducted using 4x, 10x, 20x
958 objectives. For high magnification live cell acquisition, either an Andor spinning disc confocal
959 scanhead installed on an inverted Axio observer microscope (Zeiss), using a C-Apochromat
960 63x/1.2 W Korr UV-VIS-IR objective, or a total internal reflection (TIRF) setup consisting of
961 an inverted Axio observer microscope (Zeiss), a TIRF 488/561 nm laser system (Visitron
962 systems) and an Evolve™ EMCCD camera (Photometrics) triggered by VisiView software
963 (Visitron) was chosen. Photo-activation experiments were conducted on an inverted
964 Spinning disc microscope (iMic) using a 60x/1.35 Oil objective. TAMRA stained DCs were
965 either untreated or treated with 10μM PST-1 in the dark and recorded using a 561nm laser
966 line in 2-second intervals. Photoactivation was carried out on directionally migrating cells
967 using a 405 nm laser line (pixel dwell time: 10 ms, interval: 40 sec). FRAP calibration was
968 carried out on separate samples before each experiment. During live cell imaging cells were
969 held under physiological conditions at 37˚C, 5% CO_2 in a humidified chamber. Acquisition of
970 fixed samples (*in situ* ear crawl in and immunofluorescence samples) was carried out using
971 an upright confocal microscope (LSM700, Zeiss) equipped with a Plan-Apochromat 20x/1.0
972 W DIC (UV) VIS-IR or a Plan-Apochromat 63x/1.4 Oil objective.
973

974 **Statistics**

975 All boxes in Box-Whisker plots boxes extend from 25th to 75th percentile and whiskers span
976 minimum to maximum values. Graphs represent pooled data of several cells (n) from
977 independent biological experiments (N) as mentioned in the figure legends. Individual
978 experiments were validated separately and only pooled if showing the same trend. For
979 representation of frequencies, bar charts depict mean values from several independent
980 biological experiments (N) ± S.D. Statistical analysis was conducted out using GraphPad
981 Prism.

982

983 **Supplementary References**

984 Leithner, A., Eichner, A., Müller, J., Reversat, A., Brown, M., Schwarz, J., et al. (2016).
985 Diversified actin protrusions promote environmental exploration but are dispensable for
986 locomotion of leukocytes. *Nature Cell Biology*, *18*(11), 1253–1259.
987 http://doi.org/10.1038/ncb3426

988 Lutz, M. B., Kukutsch, N., Ogilvie, A. L., Rössner, S., Koch, F., Romani, N., & Schuler, G.
989 (1999). An advanced culture method for generating large quantities of highly pure
990 dendritic cells from mouse bone marrow. *Journal of Immunological Methods*, *223*(1),
991 77–92.

992 Redecke, V., Wu, R., Zhou, J., Finkelstein, D., Chaturvedi, V., High, A. A., & cker, H. H. A.
993 (2013). Hematopoietic progenitor cell lines with myeloid and lymphoid potential. *Nature*
994 *Methods*, 1–13. http://doi.org/10.1038/nmeth.2510

995 Sixt, M., & Lämmermann, T. (2011). In vitro analysis of chemotactic leukocyte migration in
996 3D environments. *Methods in Molecular Biology (Clifton, N.J.)*, *769*(Chapter 11), 149–
997 165. http://doi.org/10.1007/978-1-61779-207-6_11

998

999

1000 **Supplementary figure legends**

1001 **Supplementary figure 1. (A)** Schematic representation of migration assays used in this
1002 study. Assays range from highly complex (top) and relatively uncontrollable geometries to
1003 very simple and precisely controllable PDMS-based structures (bottom). Complexity of the
1004 geometrical confinement correlates with dynamic shape changes of cells. Upward-facing
1005 arrows indicate high geometrical complexity and cell shape changes respectively.
1006 Downward-facing arrows indicate low complexity. **(B)** *In situ* migration of exogenously
1007 generated DCs on a mouse ear sheet. Shown are z-projections of separated ear sheets
1008 upon control (DMSO) or pharmacological treatment (Nocodazole). Lymphatic vessels were
1009 stained for Lyve-1, DCs with 7μM TAMRA before application on ear sheets. Pictures below
1010 represent z-stack of magnified region rotated around the Y-axis. Scale bar, 100μm in left
1011 images, 10μm in middle and right images. **(C)** Individual cell migration trajectories of
1012 automatically tracked DCs migrating within a 3D collagen network. Scale bar 100μm. **(D)**
1013 Non-treated (NT) or Nocodazole-treated cells migrating under agarose were fixed and
1014 stained for endogenous distribution of alpha-tubulin. Scale bar 10μm. **(E)** Time-lapse
1015 montage of a Nocodazole-treated Tubulin-GFP and membrane-targeted tdTomato
1016 expressing cell under agarose. Scale bar, 10μm. **(F)** Kymograph of DCs migrating within a
1017 straight microchannel. Cells were either untreated (NT) or Nocodazole (Noco.) treated.
1018 Scale bar 10μm. **(F)** Cell lengths of non-treated (NT), Nocodazole (Noco.) treated and
1019 double-treated cells using Y27632 and Nocodazole (Y/N) of n = 25 cells per condition from N
1020 = 3 experiments. Boxes extend from 25th to 75th percentile. Whiskers span minimum to
1021 maximum values. **** $P \leq 0.0001$.

1022

1023 **Supplementary figure 2. (A)** Time-lapse montage of cells migrating along a CCL19
1024 gradient when confined under agarose (top panel) and when fixed with 4% PFA during
1025 migration (bottom panel). Small panels below image sequences are montages of black-
1026 boxed regions over time to visualize advancement of the leading edge. The red dotted line
1027 represents the cell leading edge. Scale bar, 10μm. **(B)** Determination of MTOC position by
1028 alpha- and gamma-tubulin staining (left panels). MT nucleation from centrosomal origin
1029 visualized by line scan of signal intensities along purple line in merged image (right panel).
1030 Scale bar, 10μm. **(C)** Still images of a cell expressing EB3-mCherry and tubulin-GFP
1031 migrating under agarose. Scale bar 10μm. Right panel highlights localization of EB3 signal
1032 at the tip of polymerizing tubulin filaments as the cell advances. Scale bar 5μm. **(D)**
1033 Automatically detected EB3 comets (cyan) overlaid on maximum intensity time projection
1034 (120 sec) of an EB3-mCherry expressing cell migrating under agarose. Lower panel:

1035 Quantification of MT growth events of front (gray) vs. back (purple) directed MT tracks over a
1036 time period of 120sec of n = 7 cells. Boxes extend from 25th to 75th percentile. Whiskers
1037 span minimum to maximum values. Scale bar, 10μm. **(E)** MT growth dynamics in protrusive
1038 (gray box) vs. contractile (purple box) areas. Scale bar, 10μm. Lower panel: Differential EB3-
1039 mCherry fluorescence intensities in protrusive (front) vs. contractile (back) areas of n = 16
1040 cells from N = 3 experiments. **** P ≤ 0.0001. **(F)** Quantification of 2D projected cell area of
1041 polarized DCs expressing membrane-targeted tdTomato. Boxes extend from 25th to 75th
1042 percentile and whiskers span minimum to maximum values of n = 13 cells. *** P ≤ 0.001. **(G)**
1043 Quantification of EB3 growth events relative to the cell area. Mean ± S.D. of n = 7 cells. **(H)**
1044 Time-course analysis of MT filament dynamics of migrating DCs expressing EMTB-mCherry.
1045 Upper panel indicates leading edge area. The white arrow represents membrane protrusion
1046 and the green arrowhead represents elongating MT filaments. Lower panel indicates trailing
1047 edge area in which purple arrow represents membrane retraction and purple arrowheads MT
1048 filament depolymerization. Red line represents cell edges. Scale bar, 10μm. **(I)** Acetylated
1049 MTs in fixed migratory. Levels of acetylation were assessed by measuring mean
1050 fluorescence intensity of acetylated Tubulin along individual alpha-Tubulin filaments of (n =
1051 XY filaments per condition of N = 3 experiments) directed towards the front (gray) or back
1052 (purple). Boxes extend from 25th to 75th percentile. Whiskers span minimum to maximum
1053 values. **** P ≤ 0.0001. Scale bar, 10μm.
1054
1055 **Supplementary figure 3. (A)** Co-localization of Lfc-GFP on alpha-tubulin structures. A Lfc-
1056 GFP expressing cells was fixed while migrating under agarose and stained for alpha-tubulin
1057 distribution. Scale bar, 10μm. **(B)** Polarized distribution of Lfc-GFP in trailing edges and
1058 retracting protrusions. A double reporter cell expressing Lfc-GFP and EB3-mCherry was
1059 followed while migrating under agarose. Purple arrowhead denotes trailing edge, orange
1060 arrowhead highlights retracting protrusion followed by cell repolarization. Scale bar 10μm.
1061 **(C)** Lfc-GFP distribution upon Nocodazole treatment. A Nocodazole-treated double
1062 fluorescent reporter cell was followed while migrating under agarose. Note the absence of
1063 filamentous structures in both channels and the strong diffuse signal distribution of Lfc-GFP.
1064 Scale bar 10μm. **(D)** Time-lapse montage of a MLC-GFP expressing DC migrating under
1065 agarose towards a soluble CCL19 gradient. A cycle of migration, retraction, and pausing is
1066 shown. Scale bar, 10μm. Dotted lines indicate positions further analyzed by Kymograph in
1067 **(E)**. **(E)** Leading edge kymograph was derived from grey dotted line in leading edge region
1068 of **(D)**. Trailing edge kymograph was derived from red dotted line in trailing edge region of
1069 **(D)**. Scale bar, 5μm. **(F)** Time-lapse sequence showing spatiotemporal MLC accumulation of

1070 a *lfc*$^{+/+}$ DC **(G)** a *lfc*$^{+/+}$ DC treated with Nocodazole and **(H)** a *lfc*$^{-/-}$ DC. Purple arrowheads
1071 highlight trailing edge MLC accumulation, orange arrowheads indicate central MLC
1072 accumulation. Scale bars, 10μm. **(I)** Levels of MLC-GFP expression of *lfc*$^{+/+}$ and *lfc*$^{-/-}$ reporter
1073 cells determined by FACS analysis. The graph is representative of two experiments. **(J)**
1074 Analysis of endogenous phospho-MLC(S19) signal distribution in *lfc*$^{+/+}$ and *lfc*$^{-/-}$ DCs
1075 migrating under agarose along the anterior-posterior polarization axis. **(K)** Localization of
1076 phospho-MLC(S19) in MLC-GFP expressing migratory DCs. Graph indicates position of
1077 MLC accumulation relative to cell length of n = 20 (*lfc*$^{+/+}$) and n = 18 (*lfc*$^{-/-}$) cells from N = 2
1078 experiments. Boxes extend from 25th to 75th percentile. Whiskers span minimum to
1079 maximum values. **** $P \leq 0.0001$. Scale bar 10μm.
1080
1081 **Supplementary figure 4. (A)** Integration of the *lfc* targeting vector into genomic locus. Black
1082 boxes represent exons. The neo-lox P cassette was cloned in reverse orientation into two,
1083 replacing a *SmaI-XhoI* segment. Locations of primers used for PCR are indicated with
1084 triangles. Probes A and B were used for Southern blot detection of short and long arms,
1085 respectively. S, *Sma*I; Xh, *Xho*I; X, *Xba*I: N, *Nhe*I **(B)** Southern blot analysis. Genomic DNA
1086 from *lfc*$^{+/+}$, *lfc*$^{+/-}$ and *lfc*$^{-/-}$ mice was digested with *Xba*I and hybridized with probes B (left
1087 panel) and genomic DNA from *lfc*$^{+/+}$ and *lfc*$^{+/-}$ embryonic stem cells were hybridized with
1088 probe A (right panel). **(C)** PCR analysis of tail DNA from *lfc*$^{+/+}$, *lfc*$^{+/-}$ and *lfc*$^{-/-}$ mice. Locations
1089 of primers used for PCR are indicated with triangles in **(A)**. **(D)** Immunoblot analysis of total
1090 thymus cell lysates probed for Lfc protein content. **(E)** Cell morphologies of immature (NT)
1091 and mature (+LPS) *lfc* wildtype (upper-lane) and *lfc*-deficient (lower-lane) littermate DCs.
1092 Note the presence of multiple veils in both LPS-treated samples. **(F)** DC differentiation
1093 markers (MHC-II and CCR7) of *lfc* wildtype (blue line) and *lfc*-deficient (red line) littermate
1094 DCs compared to unstained cells (grey peak). **(G)** Endogenous MT organization in *lfc*$^{-/-}$ DCs.
1095 Cells migrating under agarose were fixed and stained for alpha- (left) and gamma-tubulin
1096 (middle). Scale bar, 10μm. **(H)** Line scans across the highest gamma-tubulin signal along
1097 the left-right axis (dashed line in **(G)**). The purple line indicates gamma-tubulin signal
1098 intensity. The black line indicates alpha-tubulin signal distribution. **(I)** Quantification of
1099 centrosome localization in *lfc*-deficient DCs of n = 117 cells from N = 2 experiments. **(J)**
1100 Levels of active RhoA upon MT disruption with Nocodazole in wildtype (*lfc*$^{+/+}$) and *lfc*-
1101 deficient cells (*lfc*$^{-/-}$) determined by luminometry. Activity levels are normalized to
1102 Nocodazole-treated wildtype samples, showing mean intensities ± S.D. from N = 3
1103 experiments. **** $P \leq 0.0001$. **(K)** Levels of MLC phosphorylation in *lfc*$^{+/+}$ and *lfc*$^{-/-}$ DCs
1104 assessed by Western Blot analysis. Cells were pretreated with the indicated compounds

1105 (DMSO, CCL19, CCL21, Nocodazole, Y27632 together with Nocodazole). Mean
1106 fluorescence intensity of phospho-MLC was normalized to GAPDH signal and shown as fold
1107 increase relative to DMSO control ± S.D. Blots are representative of N = 3 experiments. **(L)**
1108 Path choice preference of *lfc*$^{+/+}$ and *lfc*$^{-/-}$ DCs migrating within a complex path choice assay.
1109 Shown are mean frequencies of *lfc*$^{-/-}$ n = 49 cells of N = 2 experiments and *lfc*$^{+/+}$ n = 79 cells
1110 of N = 3 experiments. **(M)** Centrosome position with respect to nucleus of *lfc*$^{-/-}$ DCs migrating
1111 within a path choice assay. Shown are mean frequencies of *lfc*$^{-/-}$ n = 49 cells of N = 2
1112 experiments. **(N)** Frequencies of cell rupturing events of *lfc*$^{+/+}$ (n = 73 cells, N = 3
1113 experiments) and *lfc*$^{-/-}$ (n = 128 cells, N = 3 experiments) DCs migrating within a simple 1D
1114 single constriction channel.
1115

1116 **Supplementary movie legends**

1117 **Supplementary movie 1. Perturbation of MT and myosin dynamics impairs DC**
1118 **migration in complex 3D scaffolds.** Mature DCs migrating along a soluble CCL19 gradient
1119 within a 3D collagen matrix. Shown are separately acquired bright field movies of control-
1120 (DMSO), Nocodazole-treated and double-treated cells using Y27632 and Nocodazole (Y/N)
1121 reconstructed in a single file. Images were acquired every 60sec for 5h and are represented
1122 as single movie in 4min intervals. Time in [min:sec]. Scale bar, 100μm for representative
1123 movie of bulk cell movement, scale bar, 10μm for movie showing single cell dynamics.

1124

1125 **Supplementary movie 2. Perturbation of MT and myosin dynamics permits DC**
1126 **migration within simple 1D microenvironments.** Mature DCs migrating along a soluble
1127 CCL19 gradient within a 1D microchannel. Shown are separately acquired bright field
1128 movies of non-treated, Nocodazole-treated and double-treated cells using Y27632 and
1129 Nocodazole cells reconstructed in a single file. Images were acquired in 20sec intervals for
1130 5h. Note the frequent directional oscillations of Nocodazole only treated cells. Time in
1131 [min:sec]. Scale bar, 10μm.

1132

1133 **Supplementary movie 3. MT dynamics in migratory DCs.** Mature DC co-expressing EB3-
1134 mCherry and tubulin-GFP. Migration of a double fluorescent cell along a soluble CCL19
1135 gradient during 2D confinement under agarose was acquired in 0.5sec intervals using an
1136 inverted spinning disc microscope setup. Time in [min:sec]. Scale bar, 10μm.

1137

1138 **Supplementary movie 4. MT dynamics are polarized in migratory DCs.** DC is
1139 expressing EMTB-mCherry. Migration during 2D confinement under agarose was acquired
1140 in 2sec intervals using a TIRF setup. For representation, the signal was inverted after the
1141 acquisition. The upper panel shows the protruding leading edge, in which grey arrowheads
1142 indicate elongating MT filaments. The lower panel shows retracting trailing edge of the same
1143 cell in which purple arrowheads highlight MT shrinking events. Time in [min:sec]. Scale bar,
1144 5μm.

1145

1146 **Supplementary movie 5. Polarized MT dynamics locally activate the contractile**
1147 **module.** TAMRA stained DCs migrating under agarose were recorded every 2sec on an
1148 inverted spinning disc microscope and locally photo-activated (red box) every 40sec using a
1149 405nm laser line. Cells were either untreated (upper panel) or treated with PST-1 (lower
1150 panel). Time in [min:sec]. Scale bar 10μm.

1151

1152 **Supplementary movie 6. Polarized Lfc-GFP distribution from filamentous to diffuse**
1153 **along anterior-posterior polarization axis.** A double fluorescent Lfc-GFP and EB3-
1154 mCherry reporter cell was acquired while migrating under agarose towards a soluble CCL19
1155 gradient in 2sec intervals on an inverted spinning disc microscope. For better visualization,
1156 the signal was inverted after the acquisition. Purple arrowhead highlights persistent diffuse
1157 trailing edge Lfc-GFP accumulation during directed migration. Orange arrowhead indicates
1158 Lfc-GFP signal distribution upon protrusion-retraction. Black arrowhead indicates
1159 filamentous Lfc-GFP signal distribution in protruding areas after repolarization. Time in
1160 [min:sec]. Scale bar, 10μm.

1161

1162 **Supplementary movie 7. Lfc-GFP signal accumulation defines retraction of**
1163 **explorative protrusions.** A double fluorescent Lfc-GFP and EB3-mCherry reporter cell was
1164 acquired while migrating within a complex 3D pillar array towards a soluble CCL19 gradient
1165 in 2sec intervals on an inverted spinning disc microscope. Diffuse Lfc-GFP signal
1166 accumulation is prominent in the trailing edge (purple arrowhead) and the explorative
1167 protrusion (orange arrowhead), while the MTOC moves in a straight path towards the top.
1168 Time in [min:sec]. Scale bar, 10μm.

1169

1170 **Supplementary movie 8. Lfc specifies myosin localization at the trailing edge.**
1171 Combined movies of MLC-GFP expressing *lfc*$^{+/+}$ DCs (left panel), Nocodazole-treated *lfc*$^{+/+}$
1172 DCs (middle panel) and *lfc*$^{-/-}$ DCs (right panel) migrating under agarose along a soluble
1173 CCL19 gradient, acquired in 2sec intervals on an inverted spinning disc microscope. Purple
1174 arrowheads indicate trailing edge MLC accumulation, which is absent in *lfc*-deficient cells.
1175 Orange arrowheads highlight central MLC accumulation. Note the different time intervals of
1176 Nocodazole-treated *lfc*$^{+/+}$ DCs (middle panel). Fluorescence signal was color coded (LUT:
1177 Fire). Time in [min:sec]. Scale bar 10μm.

1178

1179 **Supplementary movie 9. Lfc regulates MT-mediated adhesion resolution.** Nocodazole-
1180 treated *lfc*$^{+/+}$ and *lfc*$^{-/-}$ DCs were acquired while migrating under agarose towards a soluble
1181 CCL19 gradient in 20 second intervals on an inverted cell culture microscope. Left panels
1182 represent Nocodazole effects on adhesive migration. Note the loss of directionality in *lfc*$^{+/+}$
1183 DCs and the pronounced elongation of *lfc*$^{-/-}$ DCs. Right panels highlight Nocodazole effects
1184 during adhesion-independent migration on PEG coated coverslips. Note the persistent loss

1185 of directionality in *lfc*$^{+/+}$ DCs but the restored cell lengths of of *lfc*$^{-/-}$ DCs. Time in [min:sec].
1186 Scale bar 100μm.
1187
1188 **Supplementary movie 10. Microtubules mediate retraction of supernumerary**
1189 **protrusions via Lfc.** *Lfc*$^{+/+}$ and *lfc*$^{-/-}$ DCs were recorded while migrating within a decision
1190 assay towards a soluble CCL19 gradient in 30sec intervals. Note that both genotypes insert
1191 multiple protrusions into different channels when reaching the junction point (black
1192 arrowheads). Red arrowheads highlight rupturing events and loss of cellular coherence only
1193 observed in *lfc*-deficient cells. Time in [min:sec]. Scale bar, 10μm.

Figure 1 - Microtubules control dendritic cells polarity

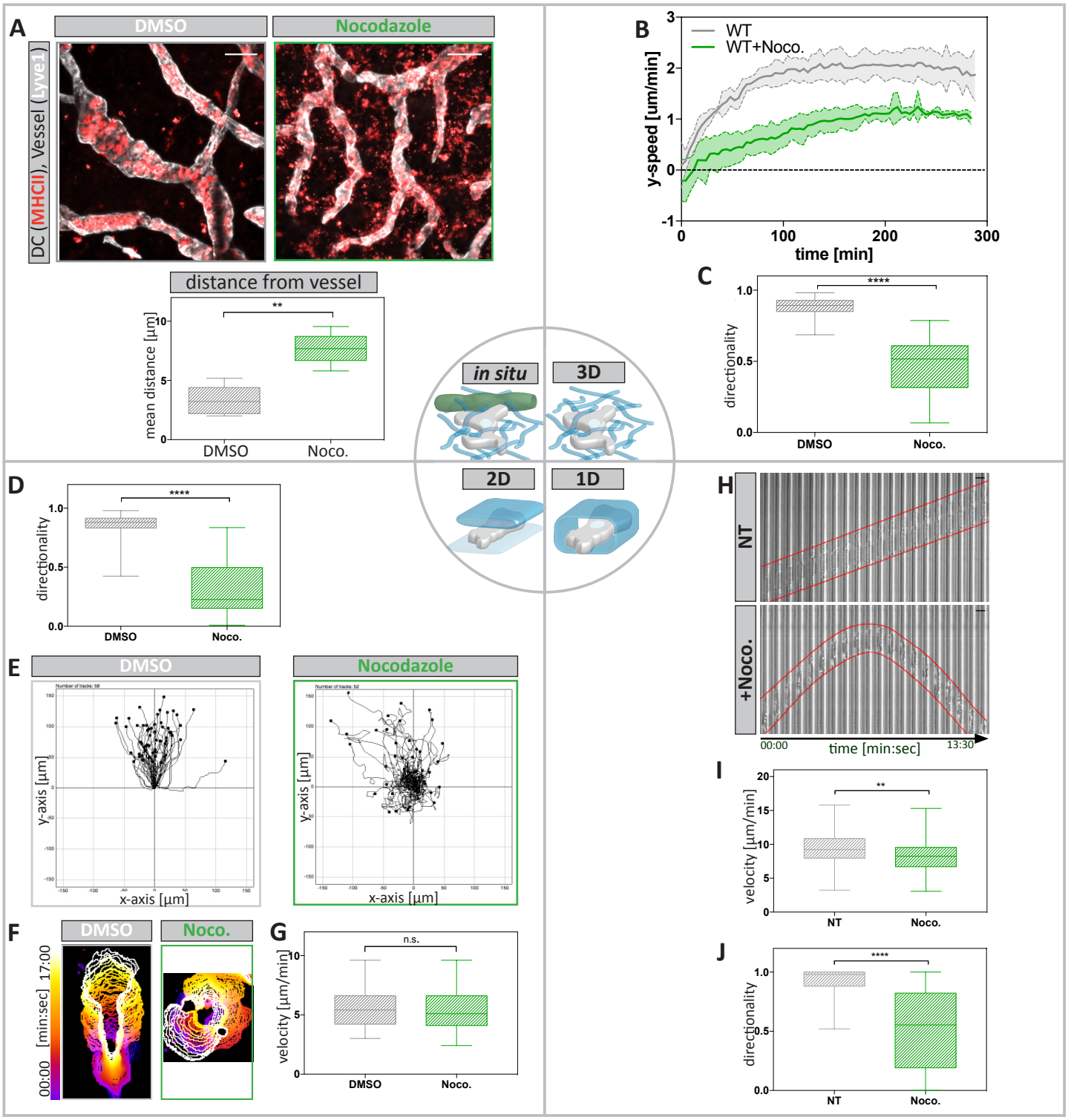

Figure 2 - Microtubules control polar cellular organization via the contractile module

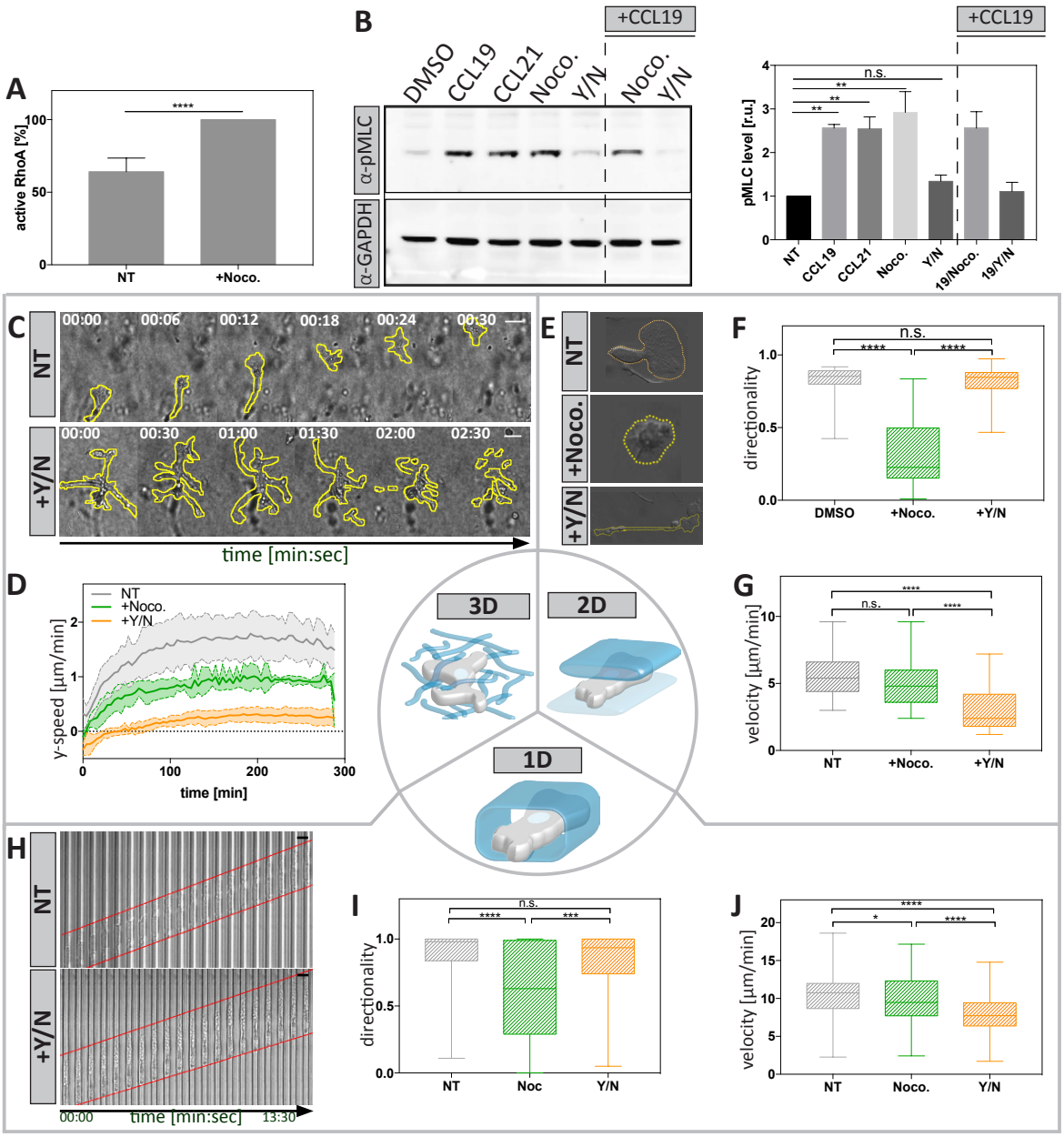

Microtubules coordinate protrusion-retraction dynamics in migrating dendritic cells

Figure 3 - Polarized microtubule dynamics locally activate the contractile module

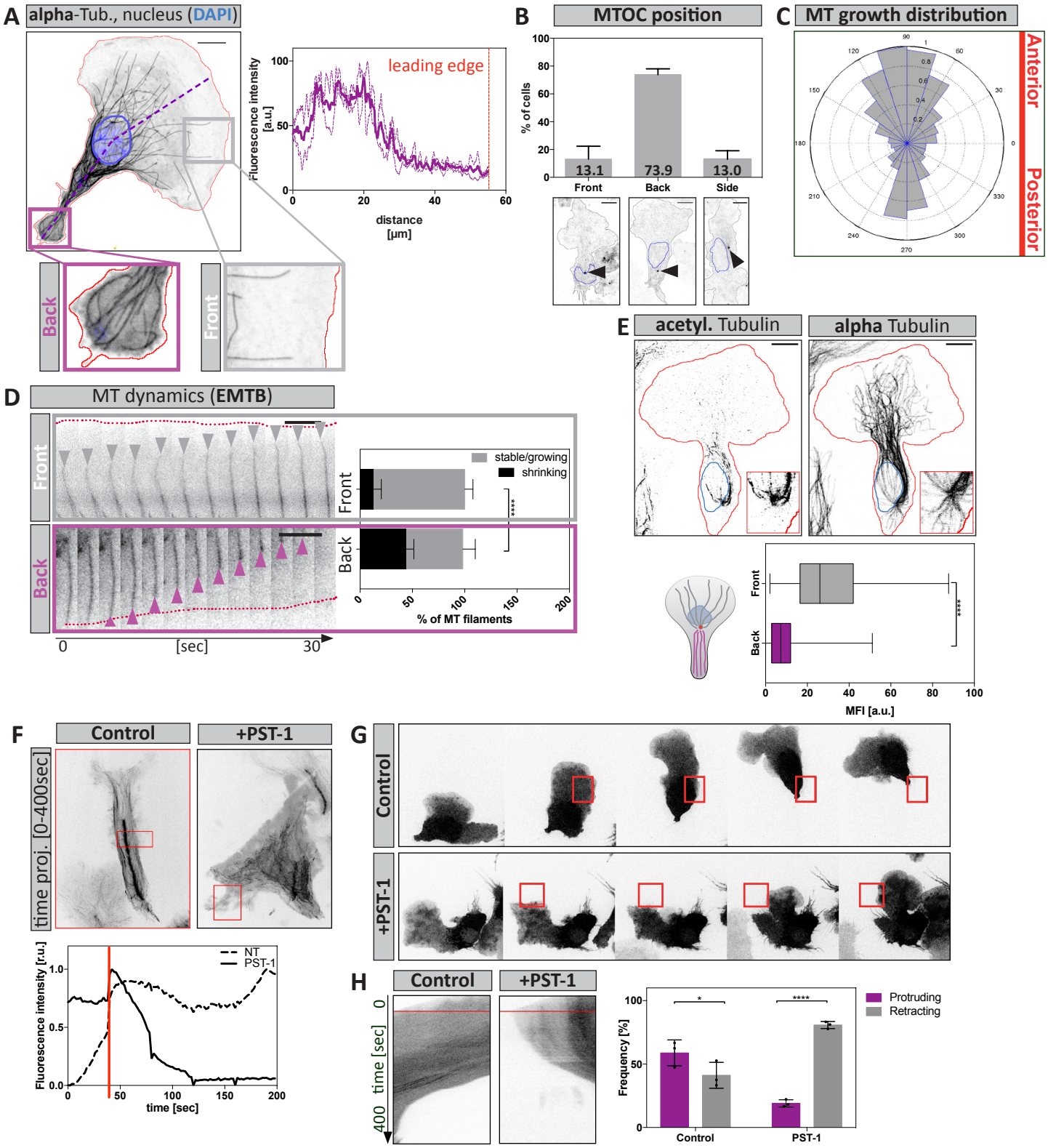

Figure 4 - Accumulation of Lfc precedes cellular retraction

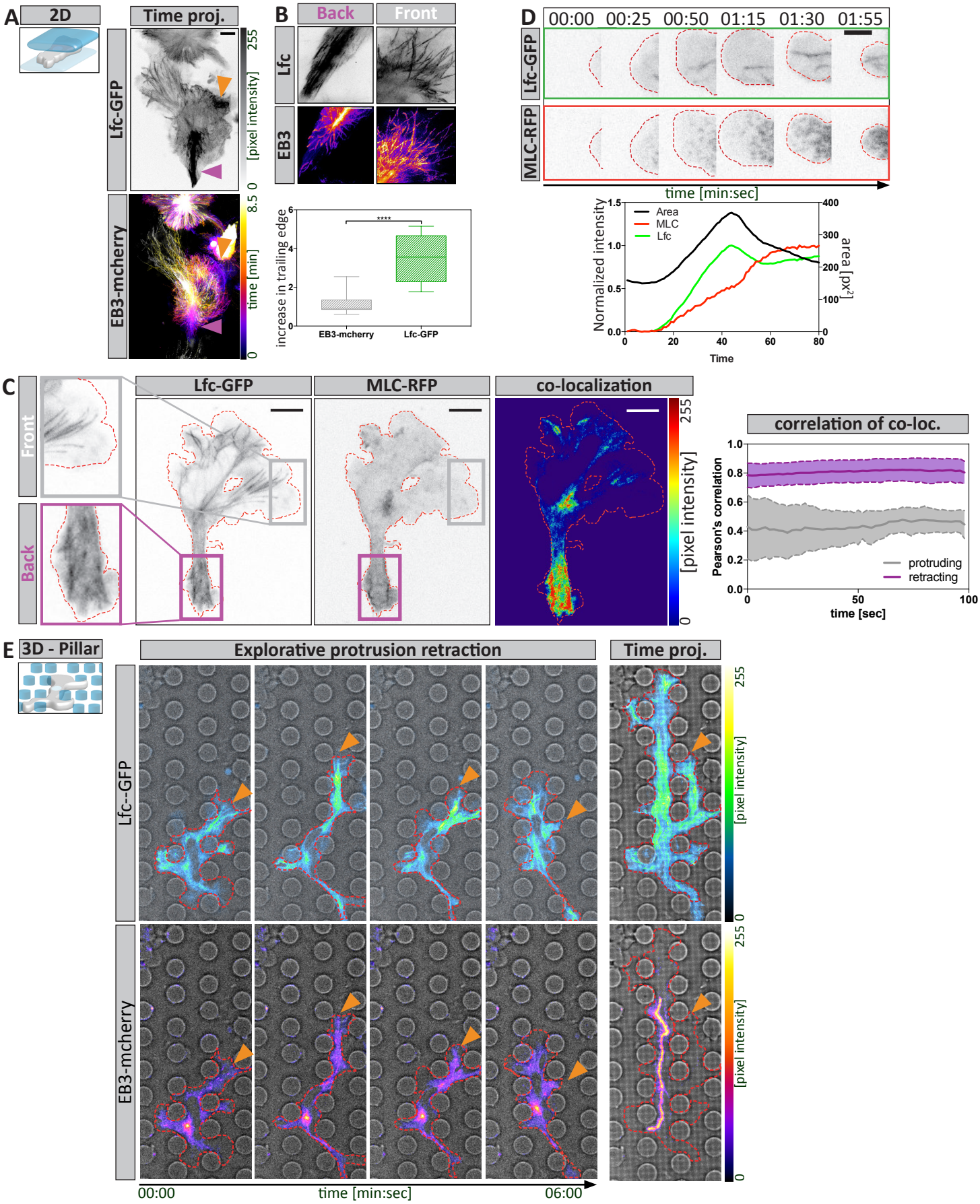

Figure 5 - Lfc specifies myosin localization at the trailing edge

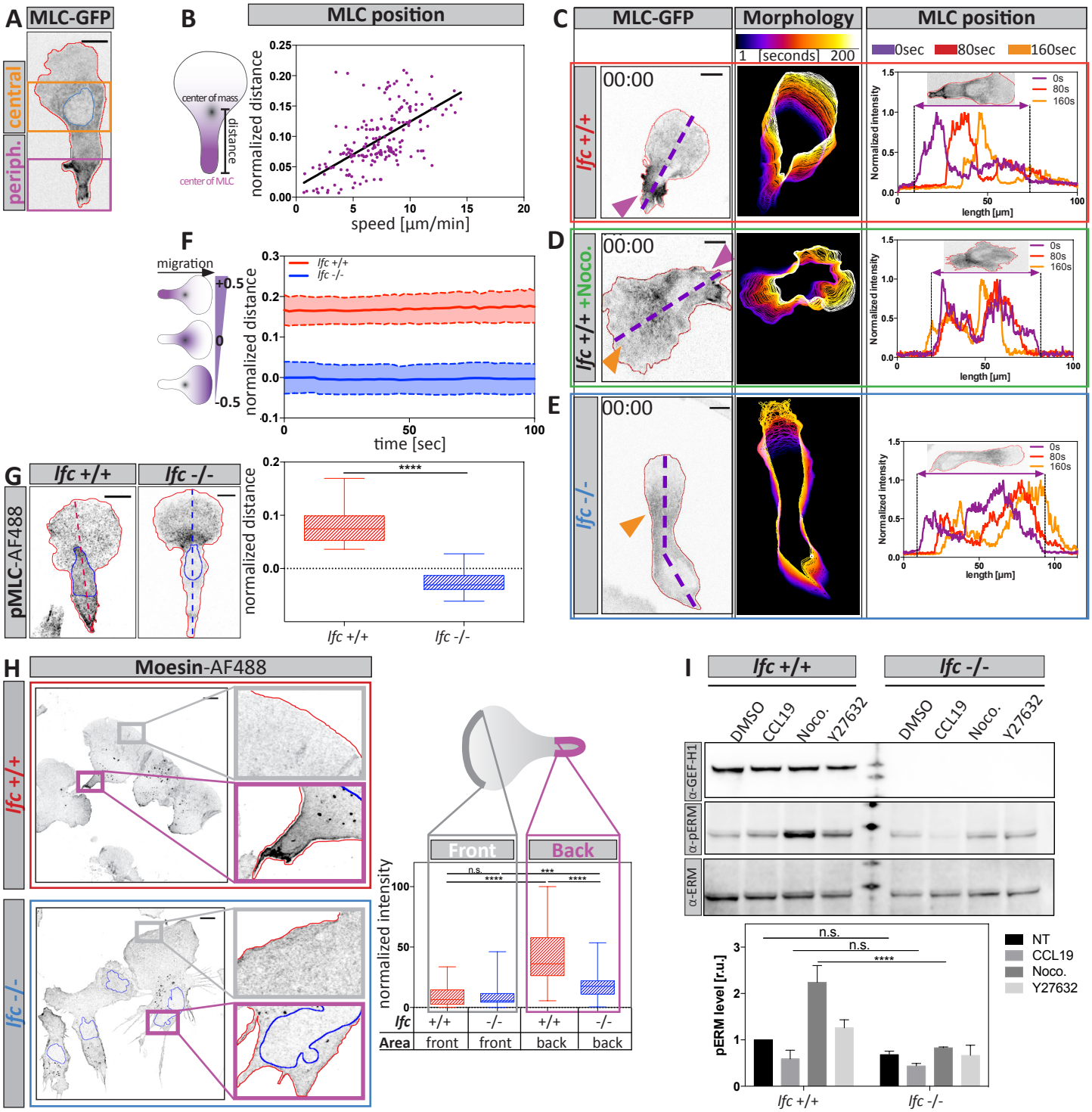

Figure 6 - Lfc controls dendritic cell migration by regulating MT-mediated adhesion resolution

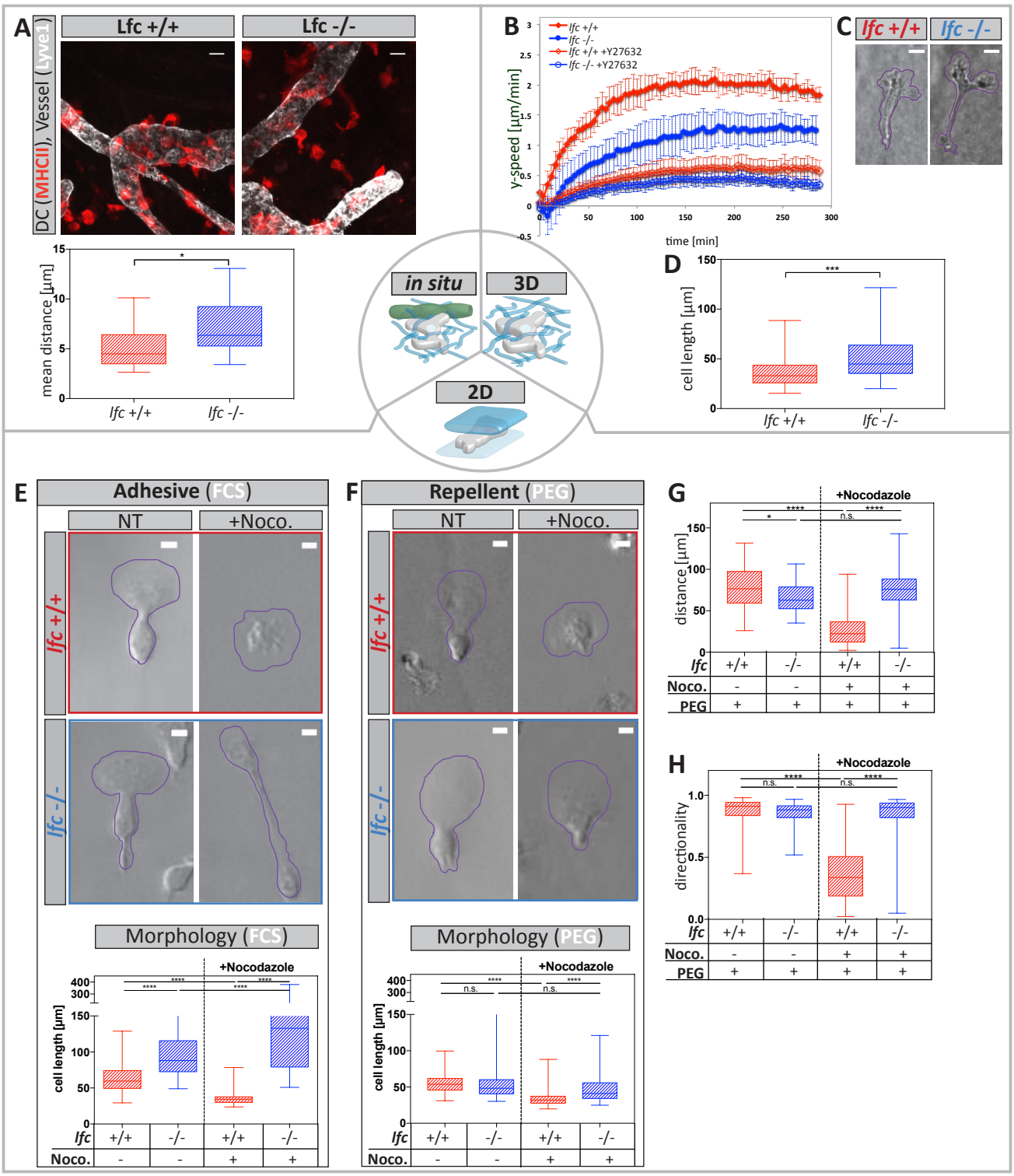

Figure 7 - Microtubules mediate retraction of supernumerary protrusions via Lfc

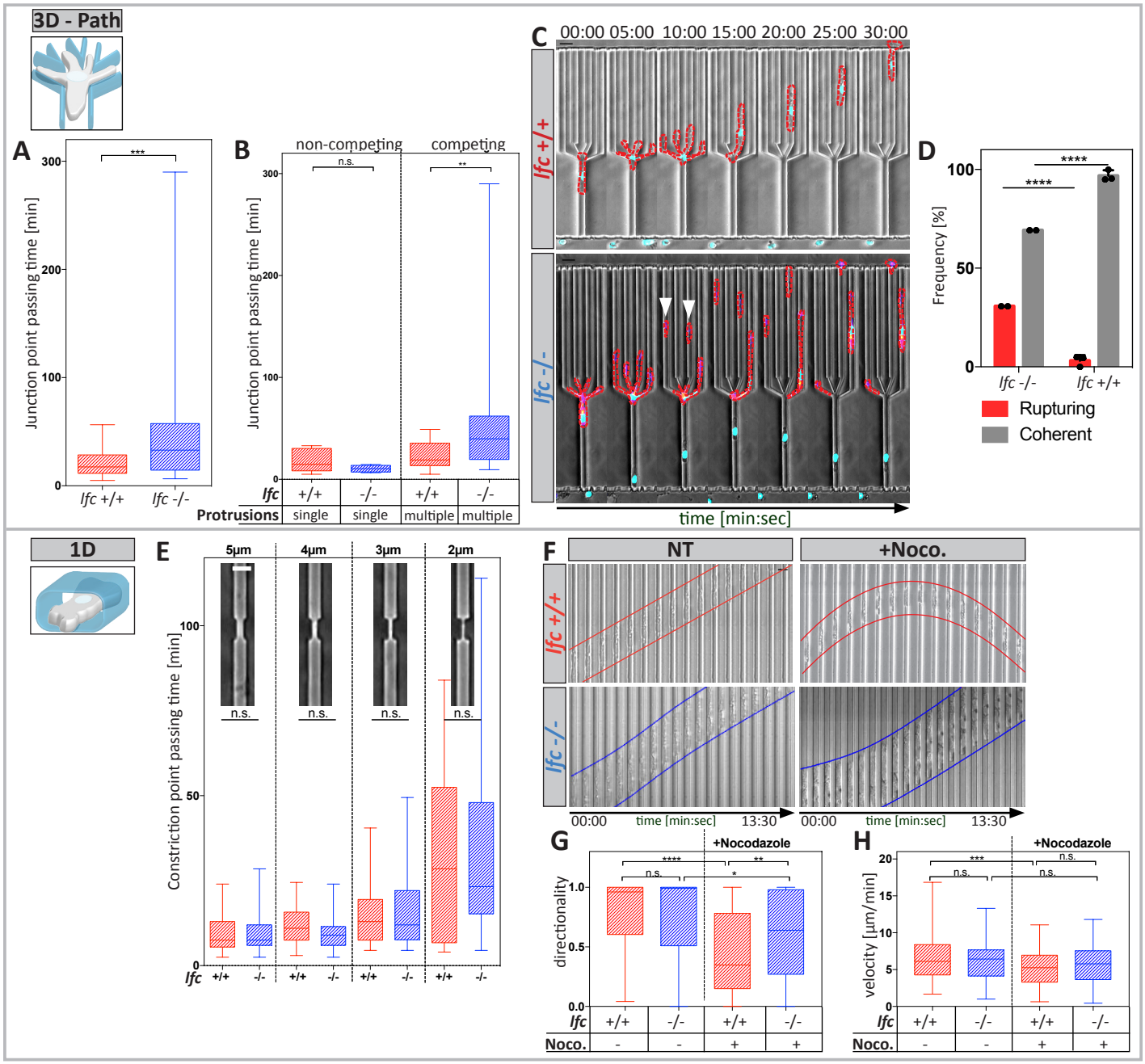

Supplementary Figure 1

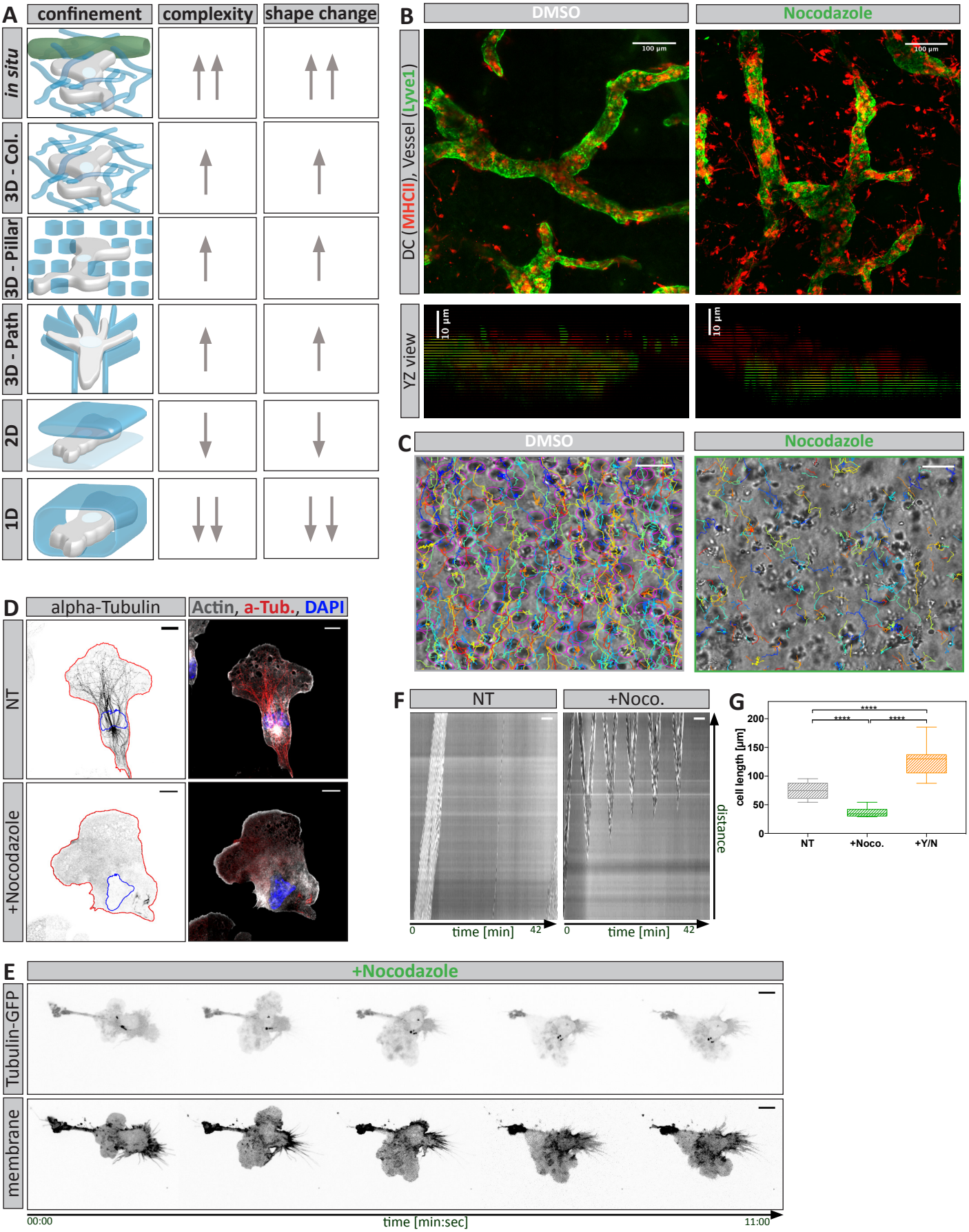

Microtubules coordinate protrusion-retraction dynamics in migrating dendritic cells

Supplementary Figure 2

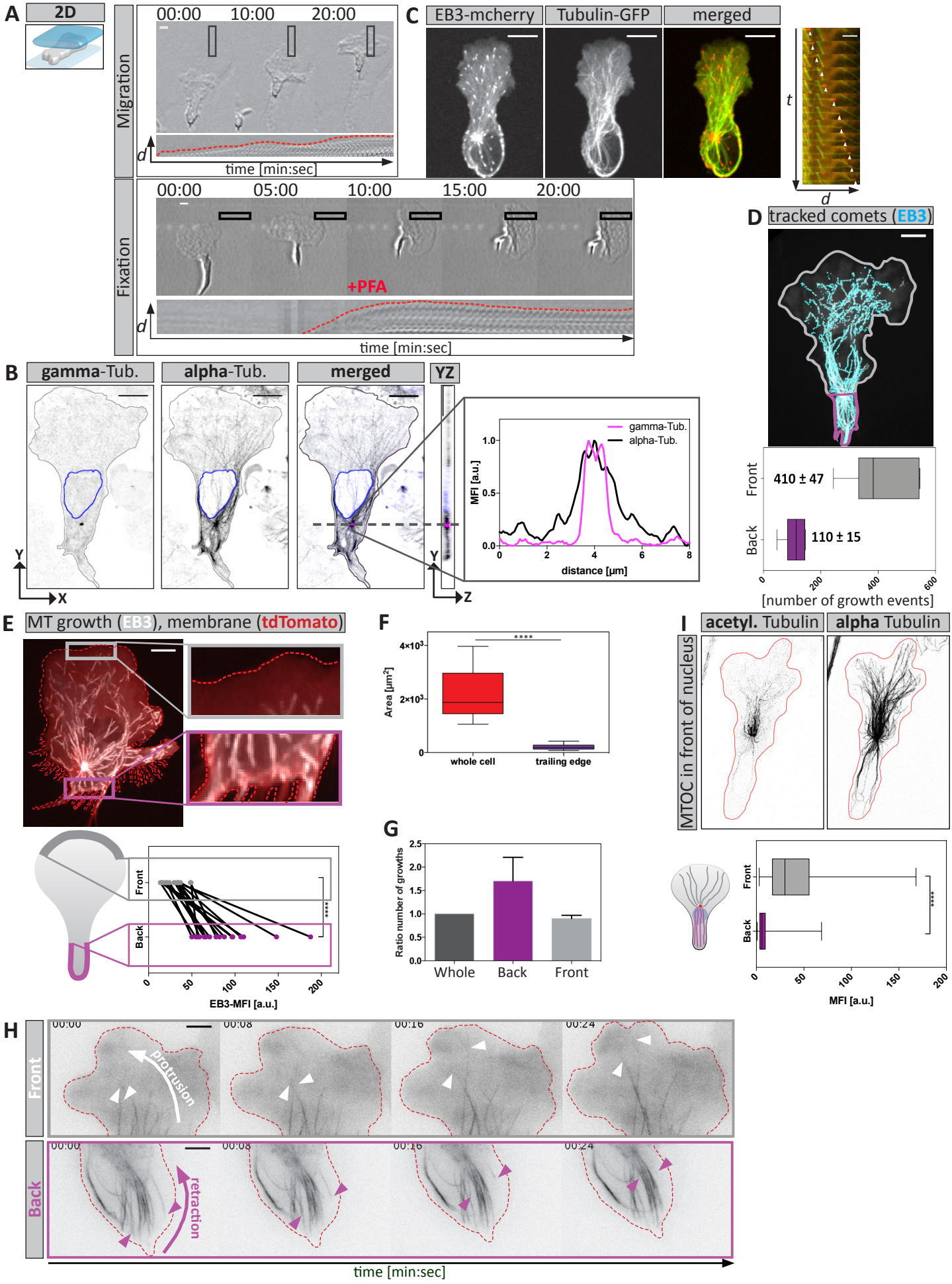

Microtubules coordinate protrusion-retraction dynamics in migrating dendritic cells

Supplementary Figure 3

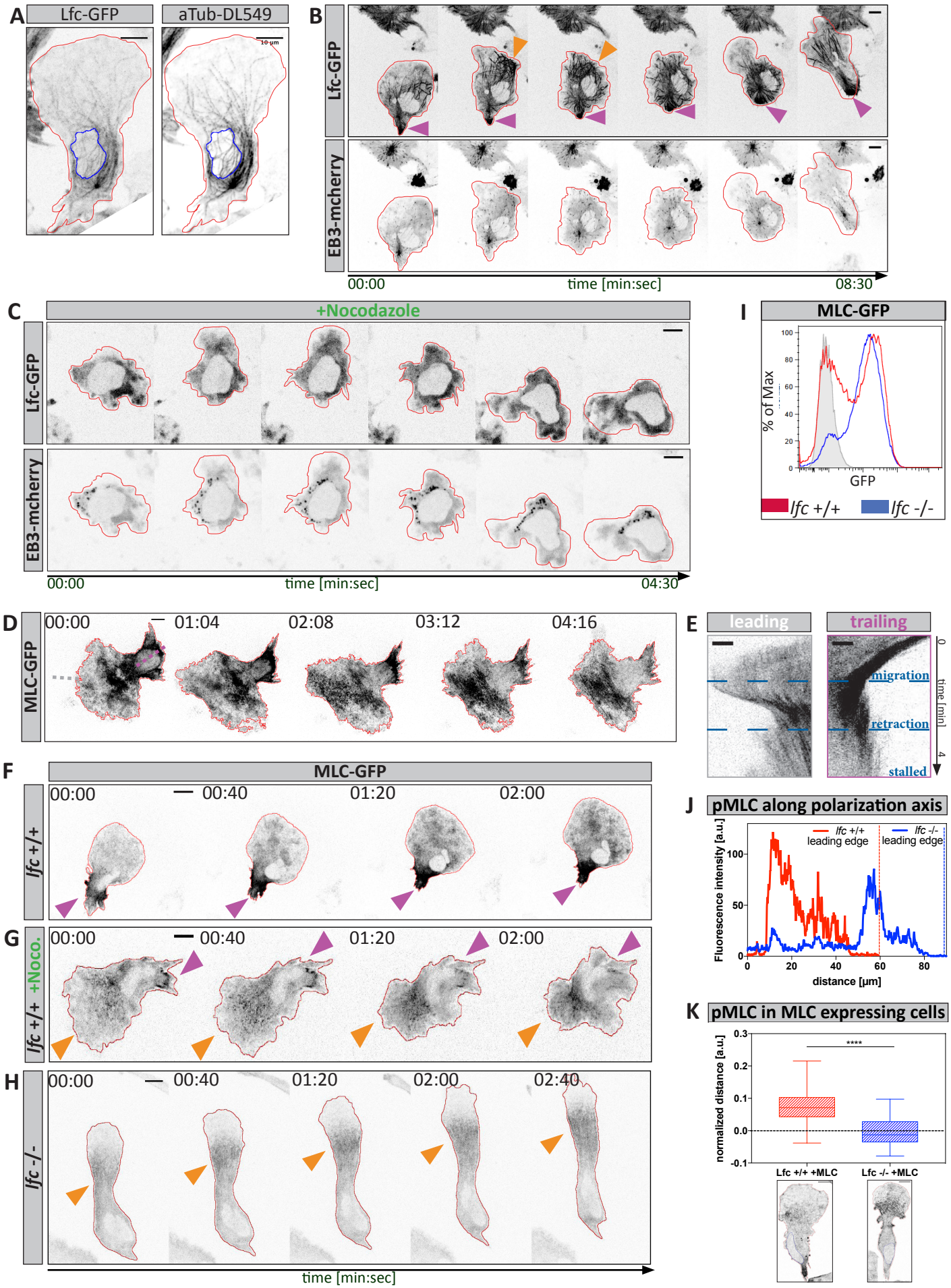
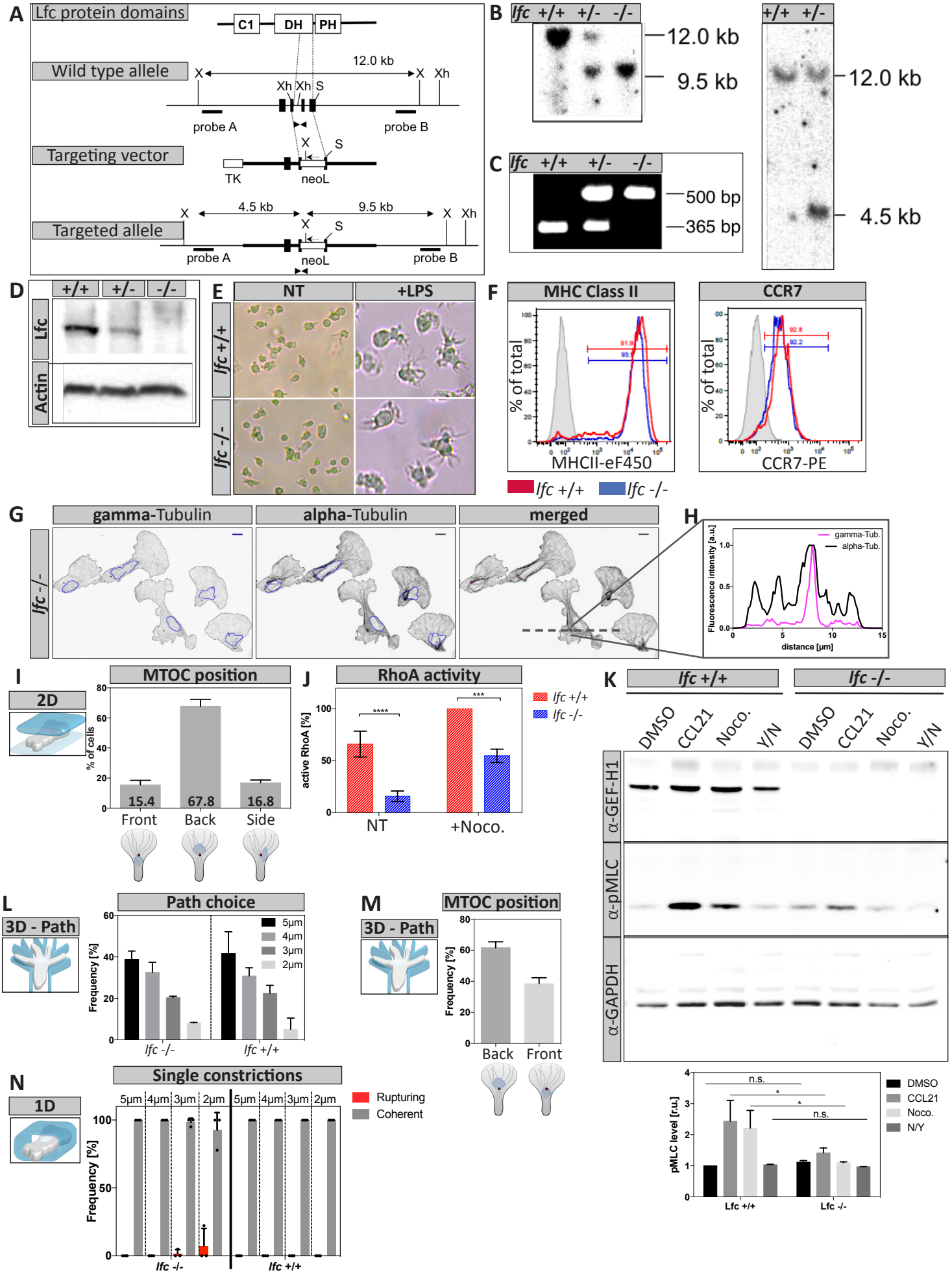
Supplementary Figure 4